Monthly Notices
of the
ROYAL ASTRONOMICAL SOCIETY

MNRAS **502,** 1947–1966 (2021) doi:10.1093/mnras/stab098
Advance Access publication 2021 January 14

Prospects for Galactic and stellar astrophysics with asteroseismology of giant stars in the *TESS* continuous viewing zones and beyond

J. Ted Mackereth,[1,2,3,4★†] Andrea Miglio,[1,5] Yvonne Elsworth,[1] Benoit Mosser,[6] Savita Mathur,[7,8] Rafael A. Garcia,[9,10] Domenico Nardiello,[11,12] Oliver J. Hall,[1] Mathieu Vrard,[13] Warrick H. Ball,[1] Sarbani Basu,[14] Rachael L. Beaton,[15,16§‡] Paul G. Beck,[7,17] Maria Bergemann,[18] Diego Bossini,[19] Luca Casagrande,[20] Tiago L. Campante,[19,21] William J. Chaplin,[1] Cristina Chiappini,[22] Léo Girardi,[12] Andreas Christ Sølvsten Jørgensen,[1] Saniya Khan,[1] Josefina Montalbán,[1] Martin B. Nielsen,[1] Marc H. Pinsonneault,[23] Thaíse S. Rodrigues,[12] Aldo Serenelli,[24,25] Victor Silva Aguirre,[26] Dennis Stello,[27] Jamie Tayar,[28†] Johanna Teske,[29,30†] Jennifer L. van Saders[28] and Emma Willett[1]

Affiliations are listed at the end of the paper

Accepted 2021 January 1. Received 2020 November 30; in original form 2020 September 4

ABSTRACT

The NASA Transiting Exoplanet Survey Satellite (NASA-*TESS*) mission presents a treasure trove for understanding the stars it observes and the Milky Way, in which they reside. We present a first look at the prospects for Galactic and stellar astrophysics by performing initial asteroseismic analyses of bright ($G < 11$) red giant stars in the *TESS* southern continuous viewing zone (SCVZ). Using three independent pipelines, we detect $\nu_{\rm max}$ and $\Delta\nu$ in 41 per cent of the 15 405 star parent sample (6388 stars), with consistency at a level of $\sim$2 per cent in $\nu_{\rm max}$ and $\sim$5 per cent in $\Delta\nu$. Based on this, we predict that seismology will be attainable for $\sim 3 \times 10^5$ giants across the whole sky and at least 10^4 giants with $\geq$1 yr of observations in the *TESS*-CVZs, subject to improvements in analysis and data reduction techniques. The best quality *TESS*-CVZ data, for 5574 stars where pipelines returned consistent results, provide high-quality power spectra across a number of stellar evolutionary states. This makes possible studies of, for example, the asymptotic giant branch bump. Furthermore, we demonstrate that mixed $\ell = 1$ modes and rotational splitting are cleanly observed in the 1-yr data set. By combining *TESS*-CVZ data with *TESS*-HERMES, *SkyMapper*, APOGEE, and *Gaia*, we demonstrate its strong potential for Galactic archaeology studies, providing good age precision and accuracy that reproduces well the age of high [α/Fe] stars and relationships between mass and kinematics from previous studies based on e.g. *Kepler*. Better quality astrometry and simpler target selection than the *Kepler* sample makes this data ideal for studies of the local star formation history and evolution of the Galactic disc. These results provide a strong case for detailed spectroscopic follow-up in the CVZs to complement that which has been (or will be) collected by current surveys.

Key words: stars: fundamental parameters – stars: oscillations – Galaxy: fundamental parameters – Galaxy: kinematics and dynamics – Galaxy: stellar content – Galaxy: structure.

1 INTRODUCTION

Asteroseismology, the study of stellar oscillations, made possible through space-based, long duration photometry of stars in missions such as CoRoT (Baglin et al. 2006; Auvergne et al. 2009), *Kepler* (Borucki et al. 2010), and K2 (Howell et al. 2014) has brought about a paradigm shift in our understanding of stellar structure and evolution. Our improved understanding of stellar interiors, driven by these missions, has led in-turn to a step-change in precision on the estimates of stellar parameters such as mass, radius, and age that can be ascertained from our analysis of observed oscillations and their comparison with detailed stellar modelling. In turn, asteroseismology provides an ideal means by which to improve and constrain such stellar models (for reviews, see e.g. Chaplin & Miglio 2013; Aerts 2019).

Stellar ages are an important aspect of the endeavour towards understanding the formation and evolution of the Milky Way, providing all important chronological contexts to these studies. Asteroseismic ages have already proven extremely useful in understanding aspects of the formation and evolution of the Milky Way disc (Anders et al. 2017b; Silva Aguirre et al. 2018; Miglio et al. 2021) and more recently, the halo (Chaplin et al. 2020; Montalbán et al. 2020). Combining asteroseismic constraints with other observational methods, such as near infra-red (NIR) spectroscopy (e.g. the APOKASC catalogue; Pinsonneault et al. 2014, 2018), have allowed for the extrapolation of asteroseismic ages on to larger samples of stars for which seismic data are not available (Martig et al. 2016; Ness

---

★ E-mail: tedmackereth@cita.utoronto.ca

† NSERC Banting Fellow.

‡ NASA Hubble Fellow.

§ Carnegie-Princeton Fellow.

et al. 2016; Ting & Rix 2018; Das & Sanders 2019; Mackereth et al. 2019). Extending the sample size and better measuring and understanding the stars in these vital training data will no doubt play a key role in the future of asteroseismology-driven Galactic studies. Such multidimensional data sets, observed by multiple surveys, also provide an ideal means by which to calibrate data between surveys.

The NASA Transiting Exoplanet Survey Satellite (*TESS*) mission (Ricker et al. 2015) was designed with a focus on the detection of nearby exoplanets (e.g. Sullivan et al. 2015). However, at the end of its 'prime' 2-yr mission, it will have provided time series photometry of stars on an all-sky basis in both targeted, short-cadence data and wide field 30-min cadence full frame images (FFIs).[1] This will increase the number of stars with detectable asteroseismic oscillations by at least an order of magnitude over *Kepler* and CoRoT (e.g. Thomas et al. 2017; Schofield et al. 2019; Silva Aguirre et al. 2020). Indeed, the asteroseismic potential of *TESS* has already been explored using early data products (e.g. Campante et al. 2019; Huber et al. 2019; Chaplin et al. 2020). The first 2 yr of *TESS* all-sky observations were taken in 27 d sectors that overlap at the ecliptic poles, forming what is referred to as the *continuous viewing zones* (CVZs), within which a complete year of continuous data has now been gathered. Stars in the CVZs are likely to have power spectra that better sample lower frequency signals than those with single sectors of data. The data for these stars can be analysed in greater detail, offering higher fidelity insights into their interiors and generating more precise estimates of their parameters.

In this paper, we present a first look at the asteroseismic constraints that are possible for stars in the *TESS*-SCVZ, based on the publicly released FFIs of the first year of *TESS* data. The SCVZ data have been fully available for over a year, providing ample time for detailed reduction of its time series data. By selecting a sample of very bright ($G < 11$) giant stars based on *Gaia* DR2 (Gaia Collaboration 2018) and 2MASS (Skrutskie et al. 2006) photometry, we demonstrate that the detection of stellar oscillations in the CVZ data across many evolutionary stages on the giant branch will allow detailed studies of stellar structure and evolution. These data will facilitate studies of the nearby Galactic stellar populations in age space, providing a strong justification for the necessity of gathering extended spectroscopic data for such samples.

In Section 2, we present the *TESS*-SCVZ bright giant sample, outlining the sample selection criteria and photometry of the FFI as well as presenting the external spectroscopic, photometric, and kinematic constraints that we use to study the properties of the sample. Section 3 presents the results of our asteroseismic analyses. There, we discuss the seismic detection yields before showing the potential of these data for stellar and Galactic astrophysics. Finally, in Section 4, we summarize our findings and make conclusions on the potential of the data set and the extrapolation of these results to the all-sky sample.

2 THE *TESS*-SCVZ BRIGHT GIANT SAMPLE

We first describe the compilation of a catalogue of stars in and around the *TESS* southern CVZ (SCVZ) for which we aim to achieve asteroseismic constraints. To this end, we select targets from *Gaia* and 2MASS, whose photometry is then extracted from the *TESS* FFIs and processed to asteroseismic power spectra. These spectra are then analysed by three independent pipelines to establish the global seismic parameters $\nu_{\max}$ and $\Delta\nu$. We complement this data with spectroscopic constraints which include the necessary stellar parameters to establish estimates of the stellar mass (and therefore age) using the Bayesian tool `PARAM` (described below). Furthermore, we include kinematic constraints that allow the inspection of this data in full six-dimensional phase space. The data set is described below, and the resulting catalogue (available online) in Appendix D.

2.1 The parent sample: *Gaia* and 2MASS data

We compile a target list of stars in and near to the SCVZ, for which *TESS* observations are now complete, by making a cone-search from *Gaia* DR2 (Gaia Collaboration 2018) within 20° of the southern ecliptic pole. We cross-match this set with 2MASS (Skrutskie et al. 2006) and select stars with $G < 11$ and parallax signal-to-noise $\varpi/\delta\varpi > 20$ (i.e. uncertainties of < 5 per cent), isolating the brightest targets with the most precise parallax measurements, for which we expect the greatest yield of asteroseismic parameters. Because we select the brightest and therefore nearby stars, we are likely unaffected by the population effects from parallax SNR selection discussed by Luri et al. (2018). We then select stars with $(J - K_S) > 0.5$ and $M_H < 3$ (estimating M_H using only the inverted parallax and ignoring the effects of extinction – although we do account for this later), isolating a final sample of 15 405 giant stars including 3019 with at least 12 sectors (27-d chunks) of data. The 'true' CVZ is within ∼10° of the ecliptic pole, so this sample includes 12 386 stars that have less than 12 sectors of data. The data in this region of the sky therefore have a wide range in dwell time and observing pattern, making it ideal for tests of data products and yields all-sky. The on-sky distribution of the stars in the input catalogue is shown in polar projection in Fig. 1. The number of sectors for which photometry was recovered is indicated by the colour of the points, demonstrating the geometric effects imposed on the data by the pointing scheme of *TESS*. Inside the CVZ, there are a number of stars with less than optimal length time series. Furthermore, the sample is clearly biased to be nearby, such that 95 per cent of targets have inverse parallaxes of $d < 1.7$ kpc. Importantly, geometric and distance selection effects may be necessary to account for in future studies that require forward modelling.

2.2 Extraction of light curves from the *TESS* FFI

We extract photometry from the *TESS* FFIs for all 15 405 stars in the target list, following the methods presented in Nardiello et al. (2019). Briefly, this method models the *TESS* PSF, accounting for spatial and temporal variations to perform photometry and neighbour subtraction (for sources between 10 and 400 arcsec from the target star) where fields are crowded. We extract light curves from the FFI using the `img2lc` code presented in Nardiello et al. (2015, 2016). The pipeline corrects for some systematic effects associated with the spacecraft, detector, and environment by modelling them using the co-trending basis vectors (CBVs) obtained by Nardiello et al. (2020). As an example, this allows for reconstruction of the light curves where a pointing problem caused a systematic loss of flux in sector 1.

The resulting light curves are then post-processed using methods outlined in García et al. (2011). Gaps in the light curves that are larger than three sectors (∼81 d) are removed, while smaller gaps are in-painted. We close up gaps longer than three sectors by concatenating the end of one sector with the beginning of the next in order to reduce the effect of the window function containing the gaps in the power spectral density (PSD). For modes that have a lifetime shorter than three sectors (90 d), the modes have been re-excited and no effect can be seen in the PSD. For modes with longer lifetimes, a break in the

---

[1] The FFI will be reobserved in the extended mission, at 10-min cadence, in the second half of 2020.

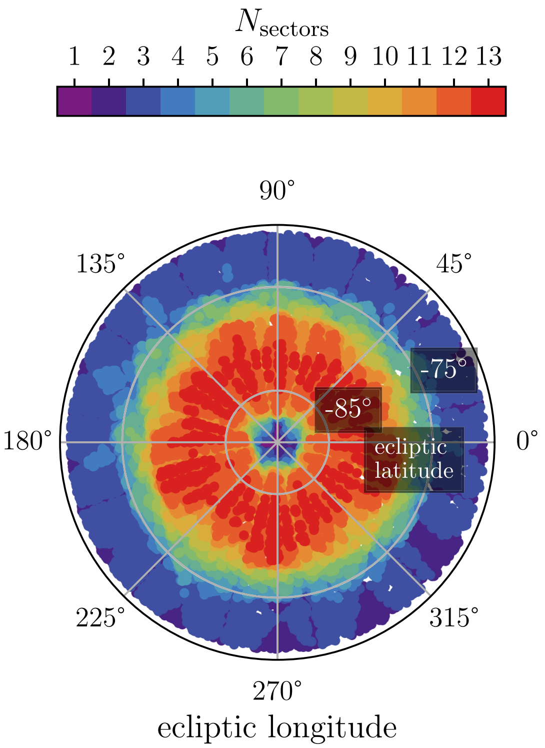

Figure 1. The *TESS*-SCVZ bright giant $G < 11$ sample in polar projection, demonstrating how the number of available sectors changes with position on sky, due to the *TESS* pointing scheme. Each camera has a 24° × 24° field of view, providing a ∼24° circular zone with many stars with 13 sectors of continuous observations. In this bright sample, many geometric selection effects are visible, due mainly to gaps in the camera CCDs.

phase is introduced (with the same effect as a stochastic excitation), which tends to slightly widen the peaks in the PSD of these modes (g-dominated mixed modes), while the frequencies are unchanged. Because we are only interested in the frequency of the modes and not in extracting the lifetimes, this methodology is justified in this case. This also removes artefacts in the data resulting from outlying data points due to target drift at the start of sectors (e.g. as the spacecraft finalized its positioning). Finally, a high-pass filter at 2 d (∼5 μHz) is applied to the time series to remove any long-term trends (this affects the detection of oscillations lower than $\nu \sim 10\,\mu$Hz). These light curves are then transformed into power spectra in frequency space using a Lomb–Scargle periodogram estimate with an oversampling factor of 10. Such an oversampling can cause small biases in the determination of seismic parameters, but this is greatly reduced for the low-frequency, stochastically excited modes in giant stars, where such oversampled spectra can improve detection statistics.

The power spectra are analysed by three pipelines to determine the global parameters $\nu_{\max}$, the frequency at maximum power, and $\Delta\nu$, the mean spacing between pressure modes of the same degree l at successive radial orders. The pipelines in question are presented in Mosser & Appourchaux (2009), Elsworth et al. (2020), and Mathur et al. (2010); we refer to them here as COR, BHM, and A2Z, respectively (similarly to, e.g. Pinsonneault et al. 2018). COR and A2Z use the power spectra for analysis while BHM uses directly the time series data. All the pipelines use independent approaches to determine the parameters, providing a means by which to assess the internal consistency in the results.

2.3 Spectroscopic and photometric parameters

In order to robustly determine useful stellar parameters such as mass and radius using the global seismic parameters, independent measures of the stellar effective temperature T_{eff} and optionally, as additional constraints, surface gravities $\log(g)$ and/or metallicity Z, are necessary. In the case of the *TESS*-SCVZ, there is little publicly available spectroscopic data from which to derive these quantities (as of the preparation of this manuscript). We demonstrate below that the gathering of detailed spectroscopy for these targets will be of great utility for the community. However, for the purposes of this 'proof-of-concept' study, we combine constraints on these quantities from the catalogue of T_{eff} and [Fe/H] derived in Casagrande et al. (2019) from the SkyMapper photometric survey DR1.1 (Wolf et al. 2018) with the *TESS*-HERMES DR1 data (Sharma et al. 2018), which provides spectroscopic constraints on $\log(g)$ (but not yet on T_{eff} or [Fe/H] for these bright giants). In total, we find that only 1186 of the 15 405 giants have all three parameters available in these catalogues. By requiring a constraint only on T_{eff} (e.g. as required when deriving the mass and radii from the asteroseismic scaling relations: Kjeldsen & Bedding 1995), the sample size increases to 8249 stars. For the stars without spectroscopic $\log(g)$ from *TESS*-HERMES, we infer a posterior on $\log(g)$ using the sample with full spectrophotometric information as a training set using the methodology described in Appendix A.

We also make use of the SDSS-IV/APOGEE-2 DR16 (Majewski et al. 2017; Ahumada et al. 2019) spectroscopic catalogue of southern stars to perform a cross-check of parameters derived using SkyMapper and *TESS*-HERMES stellar parameters. APOGEE also includes detailed element abundance information derived through the application of APOGEE Stellar Parameters and Chemical Abundances Pipeline (ASPCAP; García Pérez et al. 2016) – which uses a specifically derived linelist (Shetrone et al. 2015) – to spectra of the NIR H band taken using the twin (Southern) APOGEE spectrograph (Wilson et al. 2019) on the 2.5 m Irénée du Pont telescope at Las Cumbres Observatory (LCO; Bowen & Vaughan 1973). APOGEE spectra are then reduced and analysed using in-house pipelines (Nidever et al. 2015; Jönsson et al. 2020). Red giants in the *TESS*-CVZs are specifically targeted within APOGEE via external programme time through the Carnegie Institution of Science (PIs: Beaton, van Saders, and Teske). Information about these extra targets and more generally about APOGEE-2 targeting is presented in Beaton et al. (in preparation) and Santana et al. (in preparation). Using the APOGEE abundances, we can make some initial insights into the connections between stellar age and element abundances in the Galaxy. We find that APOGEE-2 DR16 has 513 targets in common with our bright *TESS*-CVZ giants. The SkyMapper T_{eff} and [Fe/H] generally agree well (within 1σ) with those derived by APOGEE, in the cases where both surveys returned these parameters.

We use these spectroscopic and photometric stellar parameters to determine bolometric corrections in the J, H, and K_S band for each of the targets represented in all the relevant data sets. We use the `bolometric-corrections` code,[2] which applies methods described in Casagrande & VandenBerg (2014). We then use this correction, in conjunction with the *Gaia* DR2 parallax information and the 2MASS photometry to determine the luminosity of each of the targets. The K_S-band extinction A_{K_S} is determined for each target using the `Combined19` dustmap (built from the combined dustmaps of Drimmel, Cabrera-Lavers & López-Corredoira 2003;

---

[2] https://github.com/casaluca/bolometric-corrections

Marshall et al. 2006; Green et al. 2019) implemented in the `mwdust`[3] PYTHON package (Bovy et al. 2016). We transform A_{K_S} for the J and H band using the ratios determined by Indebetouw et al. (2005). We calculate the uncertainty on the luminosity by propagating those on $T_{\rm eff}$, $\log(g)$, and [Fe/H] into the bolometric correction. Parallax uncertainties are propagated when computing absolute magnitudes. We compare the photometric luminosity with that determined from seismic parameters and scaling relations in Appendix C, and discuss this in relation to systematics in *TESS* in Section 3.1.

The parameters are then used, in conjunction with the pipeline constraints on $\nu_{\rm max}$ and $\Delta\nu$, to determine mass, radius, and age estimates for the sample via a Bayesian comparison with stellar models using the `PARAM` code (da Silva et al. 2006; Rodrigues et al. 2014, 2017). We generate results separately based on the *SkyMapper*/*TESS*-HERMES and APOGEE DR16 parameters, including both in our catalogue. `PARAM` provides full posterior information on age and mass based on the input observables (and their uncertainties). We report here and in the catalogue the median and interquartile range of the posterior distributions as our final mass, radius, and age constraints.

While `PARAM` provides a robust way to estimate mass and age based on the seismic and spectrophotometric constraints, it has a number of important caveats. Of course, any comparison to stellar models is subject to the limitations of the model predictions themselves. Similarly, the comparison between models and data is hampered by details such as the so-called surface effects that are not currently modelled and likely depend on stellar parameters in complex ways (e.g. Manchon et al. 2018). However, a number of tests have shown that this method provides accurate mass estimates to within a few per cent when compared to eclipsing binaries and clusters (e.g. Miglio et al. 2016; Handberg et al. 2017; Rodrigues et al. 2017; Brogaard et al. 2018). The `PARAM` approach also avoids the usual problems in understanding uncertainties associated with corrections to the $\Delta\nu$ scaling relation (e.g. Brogaard et al. 2018).

2.4 Stellar kinematic constraints

We obtain kinematic constraints for the sample using astrometric parameters from the *Gaia* DR2 (Gaia Collaboration 2018) catalogue. The proper motion $\mu_{[l,b]}$ and radial velocity $v_{\rm helio}$ constraints provided by *Gaia* in this bright and nearby regime are likely to be accurate, and so we apply these without correction or adjustment for zero-point offsets or biases, which are small in comparison to parameter values. The more important parallax zero-point offsets in the (now extensive) literature (e.g. Lindegren et al. 2018; Hall et al. 2019; Khan et al. 2019; Leung & Bovy 2019; Schönrich, McMillan & Eyer 2019; Zinn et al. 2019; Chan & Bovy 2020) range from $30\,\mu\mathrm{as} \lesssim \Delta\varpi \lesssim 60\,\mu\mathrm{as}$, agreeing that the raw *Gaia* DR2 values are too small. The majority of these groups consistently find an offset in the region of 50 µas. We make a simplified assessment of the parallax zero-point offset implied by our seismic results in Appendix B, finding an offset of $30 \pm 2\,\mu$as for this nearby, bright sample, which we apply externally to every star in our catalogue. This implies a $\lesssim 3$ per cent decrease in distance to the majority of the stars we consider. We defer a more detailed assessment of the *Gaia* parallax zero-point offset using *TESS* to future studies.

To propagate astrometric parameters to Galactocentric coordinates, we take 100 samples of the joint posterior of the parameters using the median, uncertainty, and correlation coefficients for each. Throughout the paper, we adopt a solar position of $[R_\odot, z_\odot] = [8.125, 0.02]$ kpc (Bennett & Bovy 2018; Gravity Collaboration 2018) and a corresponding velocity $\vec{v}_\odot = [U, V, W] = [-11.1, 245.6, 7.25]$ km s^{-1} based on the combined constraints of Schönrich, Binney & Dehnen (2010) and the SGR A∗ proper motion from Gravity Collaboration (2018). We process every sample of the astrometric parameters into the left-handed Galactocentric cylindrical coordinate frame. The resulting uncertainties on v_R, v_T, and v_z are ∼1 km s^1.

Finally, we estimate the orbital parameters $r_{\rm peri}$, $r_{\rm apo}$, e, and $z_{\rm max}$ for each sample of each star's phase-space coordinates using the fast orbit estimation method described by Mackereth & Bovy (2018) and implemented in `galpy` (Bovy 2015), adopting the simple `MWPotential2014` potential included there. We include these estimations in our final catalogue, reporting the median and interquartile range of the resulting posterior distribution of orbital parameters for each star. The median uncertainties on the final orbital parameters are less than 2 per cent.

3 RESULTS

3.1 Systematics in light curves derived from the FFI

Before looking in detail at our seismic results, we remove spurious seismic detections by comparing the luminosities computed based on the seismic parameters with those from *Gaia*. Stars that are erroneously assigned a low (high) $\nu_{\rm max}$ by any pipeline should have brighter (fainter) seismic luminosities relative to those derived directly from photometry, and so can be removed from further analysis. We perform this check by computing a 'seismic' luminosity $L_{\rm seis.}$, via the asteroseismic scaling relation for the stellar radius R,

$$\left(\frac{R}{R_\odot}\right) \simeq \left(\frac{\nu_{\rm max}}{\nu_{\rm max_\odot}}\right)\left(\frac{\Delta\nu}{\Delta\nu_\odot}\right)^{-2}\sqrt{\frac{T_{\rm eff}}{T_{\rm eff_\odot}}} \qquad (1)$$

which can then be substituted into the relationship between the luminosity and radius:

$$\left(\frac{L}{L_\odot}\right) \simeq \left(\frac{R}{R_\odot}\right)^2\left(\frac{T_{\rm eff}}{T_{\rm eff_\odot}}\right)^4 \qquad (2)$$

achieving a relationship between luminosity and the global seismic parameters

$$\left(\frac{L}{L_\odot}\right) \simeq \left(\frac{\nu_{\rm max}}{\nu_{\rm max_\odot}}\right)^2\left(\frac{\Delta\nu}{\Delta\nu_\odot}\right)^{-4}\left(\frac{T_{\rm eff}}{T_{\rm eff_\odot}}\right)^5. \qquad (3)$$

For each target where a photometric luminosity $L_{\rm phot.}$ could be estimated using the spectrophotometric parameters, we take samples of the asteroseismic parameters and $T_{\rm eff}$ assuming uncorrelated Gaussian uncertainties. We then propagate these samples through the above relationship to attain $L_{\rm seis.}$ and its associated uncertainty. Clearly, the precision and accuracy of $L_{\rm seis.}$ can be improved beyond that achievable with scaling relationships (e.g. Khan et al. 2019), but this methodology is sufficiently accurate to detect false positives.

We demonstrate the full comparison for each pipeline in Appendix C, but briefly summarize the results here. Between ∼5 and 15 per cent of targets have a seismic luminosity that is more than $3\sigma_c$ (where σ_c is defined at the uncertainties on each measurement added in quadrature) from the photometric value. The majority of problematic cases occur in bright stars, where pipelines return erroneously high $\nu_{\rm max}$ measurements. This is expected, since the frequency resolution of *TESS* is limited, making characterization of the power spectrum more difficult at low frequencies (i.e. ν

---

[3] https://github.com/jobovy/mwdust

$\lesssim 10\,\mu$Hz). As an example, for 13 sectors of data, at a $\nu_{\rm max} \sim 1\,\mu$Hz the number of independent frequency bins in the spectrum around the power envelope is ∼20. It should also be noted that the high-pass filtering applied to the light curves will strongly affect any possibility of detection below ∼10 μHz. We flag targets with $|(L_{\rm phot.} - L_{\rm seis.})/\sigma_c| > 3$ for each pipeline in our final catalogue. Such discrepancies may also be explained by unresolved binary systems (Miglio et al. 2014), which have a higher than expected apparent luminosity, while the seismology represents usually just one component of the binary. The detection of such systems requires highly precise parallax measurements, such as those for these nearby targets, which have hitherto been unavailable to seismic samples (e.g. those from *Kepler*). Similarly, we expect that there should be a large presence of wide binary systems within this sample (such as those found in *Kepler*, e.g. Godoy-Rivera & Chanamé 2018), which can be useful for calibrating independent age measurement techniques (e.g. Chanamé & Ramírez 2012).

A number of targets also have apparently spurious detections at the diurnal frequency, $\nu_{\rm max} \simeq 11.57\,\mu$Hz. We note that while many of these detections are consistent with that expected based on their photometric luminosities, at least some appear to be due to some spurious power excess at roughly this frequency. Extraction of the background signal from the FFI does appear to show such an excess, suggesting that this is due to some still existent issue with e.g. scattered light (such issues are noted in the *TESS* Data Release notes; Fausnaugh et al. 2018). To maximize the value of these data for asteroseismology, these systematics must be studied further and accounted for. Detailed analysis and correction for this is beyond the scope of this exploratory paper, and we simply remove problematic cases from our analysis.

3.2 Detection yields and seismic constraints

We first examine the yield of seismic detections for the bright SCVZ red giants in all three pipelines and determine the sample where all analyses provided consistent results for the global parameters. We compare realized yields with simple predictions, computed using the formalism presented in Chaplin et al. (2011) and updated for *TESS* targets by Campante et al. (2016) and Schofield et al. (2019), implemented for this sample as the `asteroestimate`[4] PYTHON package. The model uses *Gaia* and 2MASS photometry, the *Gaia* parallax, and time series length as input, but requires an initial estimate (or prior) on stellar mass. Assuming the simple scaling for the oscillation amplitudes as in Chaplin et al. (2011), mass has a limited impact on the detectability of the oscillations. More complex relationships have now been demonstrated in the literature, (e.g. Samadi et al. 2012; Corsaro et al. 2013; Yu et al. 2018), however since the uncertainty on the predicted $\nu_{\rm max}$ is likely already large, we adopt the simpler relationship. We use the PARSEC stellar evolution models (Bressan et al. 2012; Marigo et al. 2017) to determine a prior on the stellar mass by comparison with the 2MASS photometry of each star, as well as computing the yield assuming a fixed mass $M = 1.1\,{\rm M}_{\odot}$. Since these give similar results, we focus below on the statistics based on the mass prior from PARSEC. Importantly, we also model the effects of dilution or ‘wash-out’ of the asteroseismic signal of the target star by the oscillations of other stars in the photometric aperture following Campante et al. (2016). (This may also be referred to as ‘crowding’.) We implement this by finding the ratio of flux of all stars inside each target aperture in *Gaia* DR2 (down to $G = 17$) to that of the target star. This ratio, D, is then factored into the expressions for total mean mode power and granulation power when estimating the probability of detection (see equations 5 and 12 in Campante et al. 2016).

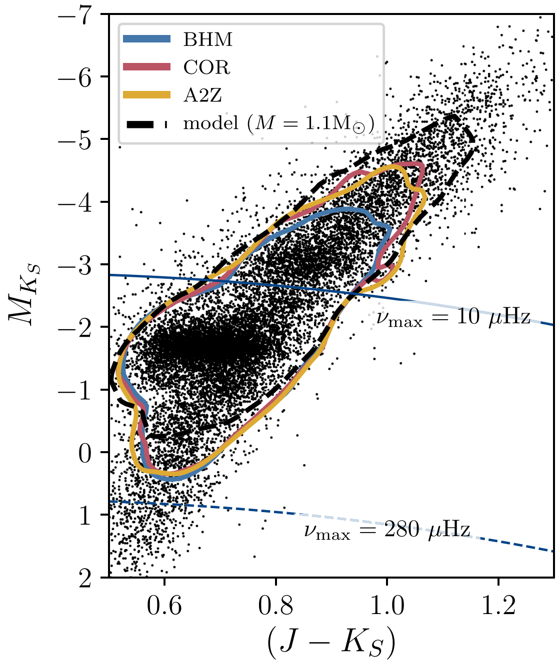

Figure 2. M_{K_S}–$(J - K_S)$ of the *TESS*-SCVZ bright giant sample. The contours demonstrate the regions in this space that contain 90 per cent of the detections made by each of the pipelines (confirmed using photometric luminosities) and a model for the detection yield based on Chaplin et al. (2011) and Schofield et al. (2019) (described further in the text). The boundaries where $\nu_{\rm max}$ is equal to 10 and 280 μHz for a 1.1 $\rm M_{\odot}$ star. 10 μHz is likely the limit at which our light curve processing might affect detections and 280 μHz is roughly the Nyquist frequency of TESS. The *TESS*-SCVZ CMD has a number of important features, such as a prominent RC at $M_{K_S} \simeq -1.5$, a clear RGB extending over the full range in M_{K_S} and the AGBb at $M_{K_S} \simeq -3$. Each pipeline makes asteroseismic detections across all of these evolutionary stages.

We define all detection yields as the fraction of stars out of the 8249 with *Gaia*-based luminosity estimates that had successful detections of $\nu_{\rm max}$ *and* $\Delta\nu$ that were confirmed using photometric luminosities. The fiducial model, accounting for the time series length and dilution effects predicts an average detection yield of ∼46 per cent. The overall detection yield over the seismic pipelines is ∼36 per cent (∼2890 stars) across the whole sample. However, the mean observed yields are ∼50 per cent for stars with the full 13 sectors of data. We find that there are 6388 stars (41 per cent of the entire 15 405 star parent sample, and 1693 of which are in the ‘true’ CVZ) that had detections in common, but not necessarily consistent, between all three pipelines. Below, we define a ‘gold’ sample from the subset of these stars, for which the global parameters were highly consistent.

Fig. 2 demonstrates the colour–magnitude diagram (CMD) of the *TESS*-SCVZ bright giant sample. The coloured contours demonstrate the regions that contain approximately 90 per cent of the stars with detections in each pipeline. The black dashed line shows the region containing 90 per cent of the stars that had a high detection probability in our fiducial detection model with dilution. Each pipeline covers a region of the CMD that contains a number of interesting features,

---

[4] https://github.com/jmackereth/asteroestimate

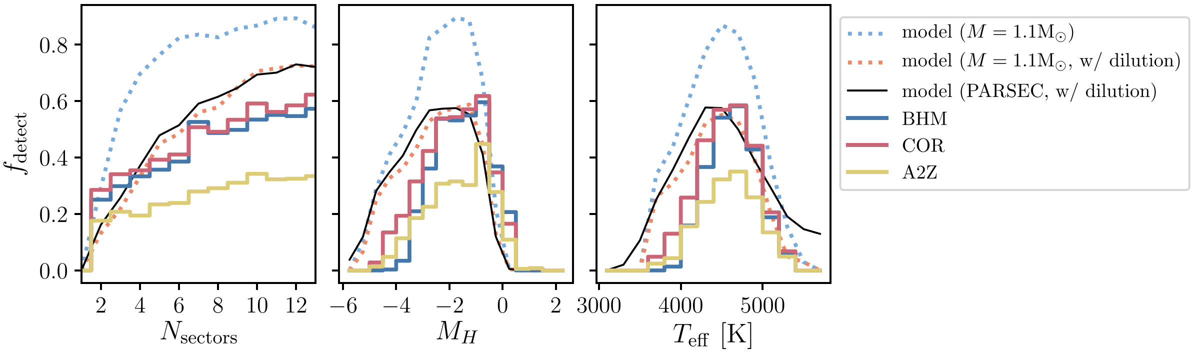

Figure 3. The detection yield $f_{\rm detect}$ as a function of the number of sectors $N_{\rm sectors}$, absolute H-band magnitude M_H and effective temperature $T_{\rm eff}$ from SkyMapper. The coloured histograms show $f_{\rm detect}$ for each pipeline considered, based on photometrically confirmed detections (see Appendix C). The dotted curves show the model yield (as in Fig. 2) assuming a stellar mass $M = 1.1\,{\rm M}_\odot$ not including (blue) and including (orange) dilution effects (see text), respectively. The solid black curve shows the predicted yield (including dilution) when intrinsic stellar parameters are sampled by comparing the 2MASS photometry with the PARSEC isochrones. The observed detection yield has a relatively low dependence on the number of sectors, but has a clear peak in M_H and $T_{\rm eff}$, where the oscillation modes are detected best.

such as the red clump (RC), giant branch, and asymptotic giant branch bump (AGBb; these are discussed more specifically in Section 3).

Fig. 3 shows the yield $f_{\rm detect}$ for each pipeline (coloured histograms) as a function of number of sectors observed $N_{\rm sectors}$, absolute H-band magnitude M_H and effective temperature $T_{\rm eff}$ (from SkyMapper). The coloured dashed curves show the expected yield from the detection models with and without dilution. The solid black curve shows the predicted yield for the fiducial model based on the PARSEC mass prior including dilution. While the details and performance of the individual pipelines are discussed in their respective papers, it is worth noting that they generally agree in terms of where the greatest yields can be achieved. It is clear that there is a range in M_H and $T_{\rm eff}$ where the global seismic parameters can be readily measured, between $-4 \lesssim M_H \lesssim 0$ and $4000 \lesssim T_{\rm eff} \lesssim 5000$, consistent with the expected range from the model. Not allowing for dilution leads to an additional ∼20 per cent predicted yield in all cases, suggesting that the large pixel size of *TESS* negatively affects seismic yields, as expected. Evidently, from Figs 2 and 3, the pipelines perform best for less evolved giants, which are fainter and hotter. These stars were more abundant in the *Kepler* sample, where these pipelines have been well tested. The effect of the high-pass filtering applied to the light curves likely also biases our analysis against the brighter giants which are predicted to have detectable oscillations.

Small differences due to population effects are evident between the PARSEC prior and the fixed mass yield models. Higher mass targets are slightly underdetected relative to lower mass stars (this will change depending on the adopted scaling relation for $A_{\rm max}$). Proper modelling of these effects will be of particular importance, for example, when trying to ascertain the Galactic star formation history based on asteroseismic samples from *TESS*, as it will impose a bias on the derived seismic age distribution against younger (and therefore more massive) targets. However, the simpler target selection of this sample makes this inherently possible, as the simple selection in colour–magnitude space is invertible using stellar population models.

We make a brief check of the internal consistency between the measurements of the global seismic parameters of the pipelines considered here in Fig. 4. We compare the results from the COR and A2Z pipelines to those from BHM to assess which, if any, pipelines are internally consistent. The summary statistics are shown in the upper left of each panel. The left-hand panels reveal that in general the pipelines agree on $\nu_{\rm max}$ at a level of 3–4 per cent, with no significant offsets from the global mean. The average consistency in $\Delta\nu$ is smaller between COR and BHM, at a level of ∼2 per cent, but is hampered between A2Z and BHM due to a set of RC giants whose $\Delta\nu$ measures are significantly different. We find similar inconsistencies between COR and A2Z. There is, however, still a core set of stars for which this parameter is consistent at the <2 per cent level (indicated by the dashed grey lines in each panel). It is conceivable that $\Delta\nu$ measures should suffer for shorter time series data. However, we find that the stars with $N_{\rm sectors} < 3$ are consistent at a similar level to those with $N_{\rm sectors} = 13$. This likely indicates some issue in definition of $\Delta\nu$ between pipelines, or some systematic issue in our *TESS* light curves that is affecting this measurement in the A2Z pipeline. For example, with few detectable orders, the definition of $\Delta\nu$ as the mean or median frequency spacing or some other weighting of these separations becomes important. Pipelines tend to differ in this regard and so may return significantly different results. The effect of this is clearly seen as larger inconsistency at low $\langle\Delta\nu\rangle$, and indeed in $\nu_{\rm max}$, in Fig. 4. Extending the time series with data from the extended *TESS* mission will improve the data in this regard, but there is almost certainly fine-tuning that still needs to be applied to achieve the best results from all pipelines.

To determine a sample of stars where all pipelines return consistent parameters, we compute the global mean of parameter measurements in cases where parameters were returned from all three pipelines. There are 5574 stars (1521 in the 'true' CVZ) for which the parameter measurements from all pipelines were consistent with the global mean within their combined uncertainty. This subset is somewhat reduced from the 6388 stars with detections in all pipelines. Much of this is driven by inconsistencies in $\Delta\nu$ noted above. The relatively large number of stars entering this 'gold' sample indicates that the pipelines are estimating uncertainties well. As an example, the median combined uncertainty on $\nu_{\rm max}$ is 1.73 μHz or ∼5 per cent. For $\Delta\nu$ the median uncertainty is 0.12 μHz, or ∼3 per cent. Determinations of $\Delta\nu$ from individual pipelines generally have lower uncertainties than the mean values. For the remainder of the paper, we choose to use the BHM values as standard in order to demonstrate the prospects for *TESS*, since these were the results with the greatest consistency with the COR pipeline. The selection of a single pipeline does not significantly affect the results of the following sections, but BHM makes a natural choice since its measured $\Delta\nu$ is defined similarly to that derived for the stellar models (Elsworth et al. 2020).

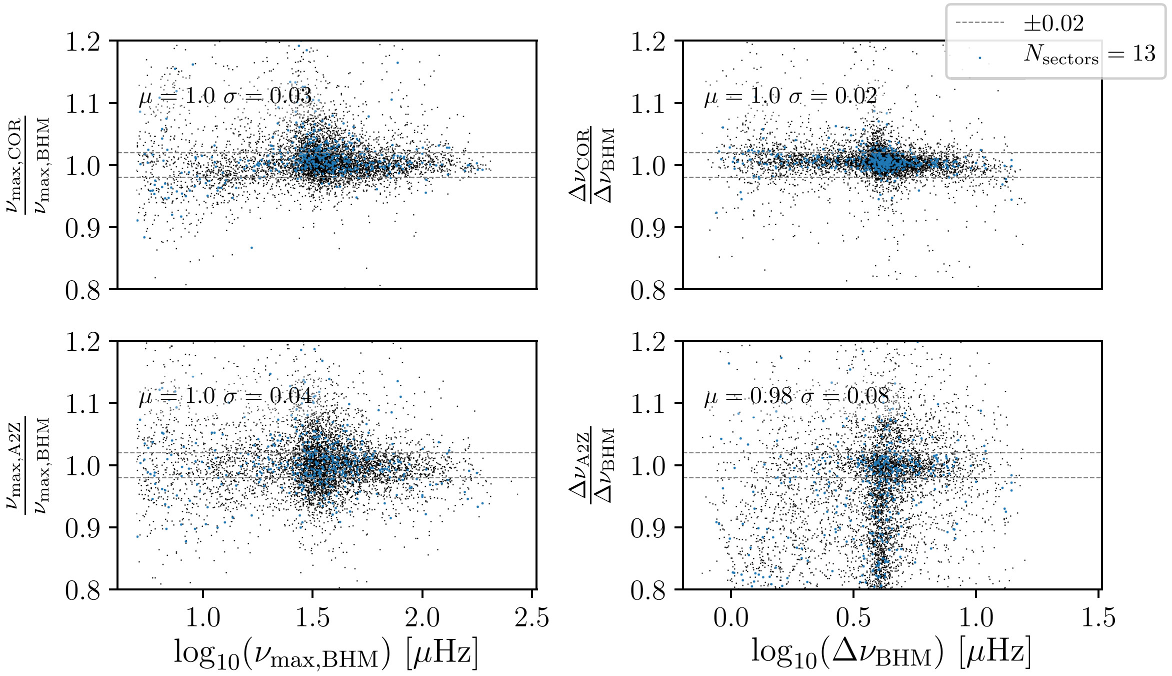

Figure 4. Internal consistency between pipelines. Left-hand panels compare the ν_{max} returned by the COR and A2Z pipelines to the measurement from the BHM pipeline. Right-hand panels show the same for $\Delta\nu$. Only stars for which results were returned in both relevant pipelines are shown. We highlight stars that have the full 13 sectors of data from *TESS*. The mean and standard deviation of the marginalized distributions are shown in the top left of each panel. In general, any differences are on the few per cent level.

Furthermore, in testing, we find that there is little difference (less than $\sim 0.3\sigma$) between the $\Delta\nu$ values returned by BHM and those catalogued by Yu et al. (2018) for stars in the *Kepler* field. The Yu et al. (2018) results agree very closely with those from individual mode frequencies and so are a good benchmark (Khan et al. 2019). Despite this selection, we still include the global mean values and the seismic gold sample identifier in our published catalogue (see Table D1 in Appendix D), recommending these stars as a benchmark for the *TESS*-SCVZ, but noting that these early values should be used with certain cautionary steps, also outlined briefly in Appendix D.

3.2.1 *Galaxia model*

We assess the future potential for seismic samples using *TESS* data with a simple model of the SCVZ generated using `Galaxia` (Sharma et al. 2011). `Galaxia` generates realistic stellar populations with realistic spatial distributions by sampling from a density model fit to Milky Way data and stellar models. For the model, we compute the 2MASS and *Gaia* photometry using `bolometric-corrections`. We then compute the detection yield in the model using the procedure above (using the stellar parameters given by `Galaxia`), extending the sample down to fainter magnitudes to gain an insight into the statistics available for fainter G magnitude stars. Again, we include dilution by other sources within the target apertures. We use the parameters provided by the stellar models in `Galaxia` (which are derived from the PARSEC library; Bressan et al. 2012; Marigo et al. 2017; Rodrigues et al. 2017) to estimate ν_{max} for each star in the model via the usual asteroseismic scaling relations and use the mass provided as input to `asteroestimate`.

Fig. 5 summarizes the statistics from our `Galaxia` model in comparison with our realized and modelled yields. The top panel demonstrates the range of ν_{max} for which seismic detections are theoretically possible as a function of G, compared to those detected by the BHM pipeline (we note that this range is nearly identical for all pipelines). Our model predicts detections down to well below $\nu_{\mathrm{max}} < 10\,\mu$Hz for the $N_{\mathrm{sectors}} > 11$ data. Extending the sample to fainter magnitudes than the currently adopted $G = 11$ limit (demonstrated by the vertical dashed line) will require better characterization of these intrinsically low ν_{max} targets. At fainter magnitudes, the observable giants are dominated by intrinsically bright (and therefore low ν_{max}) upper RGB and AGB stars. For stars with $N_{\mathrm{sectors}} = 1$, the predicted detectable range of ν_{max} is significantly decreased, owing to the fact that low-frequency oscillations are not well sampled by the shorter time series.

The lower two panels of Fig. 5 demonstrate the attainable detection yields (middle panel) and absolute sample size (lower panel) predicted by the `Galaxia` model in our adopted magnitude range, and at fainter magnitudes. The middle panel compares the predicted yield from `Galaxia` for different N_{sectors} (fine dashed lines) with those realized from our pipelines and predicted by the model based on observations. The solid curves show the cumulative fraction of detections as a function of G, indicating the fraction of all possible detections made at each G limit. At faint $G \gtrsim 9$, the realized yields agree well with those from `Galaxia`, suggesting that yield predictions based on the `Galaxia` model at fainter magnitudes are trustworthy. The yield turns over strongly at $G > 11$, suggesting this is roughly the limit for detectable giants in *TESS*. The `Galaxia` model suggests that there are many detectable brighter giants, however. The absolute cumulative detection counts shown in the lower panel also reflect this. It is likely that least some of these bright stars may be missed in our parent sample due to selection effects in *Gaia* (Boubert & Everall 2020) and our own imposed limits on parallax SNR, for example. Analyses of bright targets in *Kepler* have shown that such

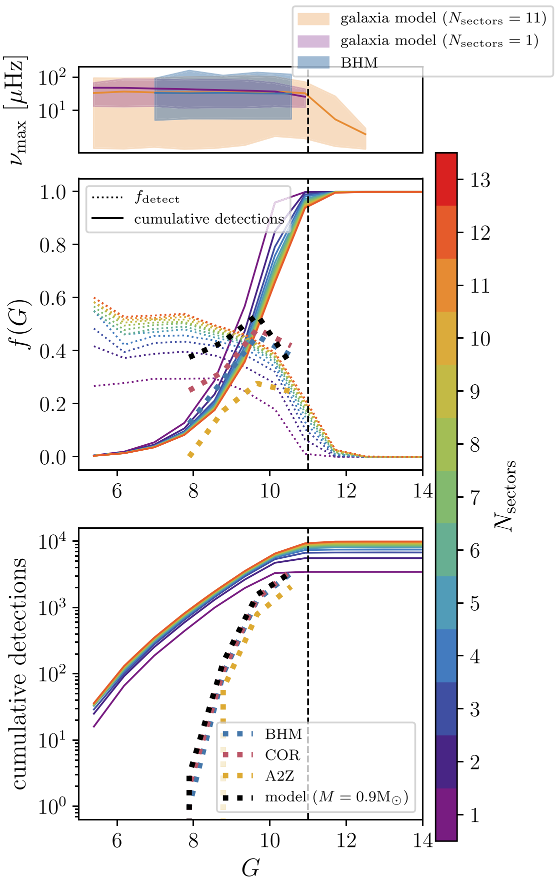

Figure 5. Detection statistics from a `Galaxia` model of *TESS*-SCVZ giant stars selected using the same photometric cuts as our giants, compared to the realized detection yields (and predictions) of the observed bright giants. The top panel shows the predicted detectable and observed (by the BHM pipeline) range of $\nu_{\rm max}$ as a function of G and for $N_{\rm sectors} = 1$ and 11. The middle panel shows the detection yield $f_{\rm detect}$ (dashed lines) and cumulative fractional detections (solid lines) as a function of $N_{\rm sectors}$. The lower panel gives the absolute cumulative number of detections as a function of G. We compare the model yields with the observed and predicted yields based on our observational sample, which are shown by the wide dashed lines (coloured as in Figs 2 and 3) in the lower two panels.

stars require specialized reduction (White et al. 2017), and this is likely also true for *TESS*.

This simple model demonstrates that somewhat increased seismic sample sizes are attainable at fainter magnitude limits, albeit at the cost to the detection 'hit-rate'. Based on our observed yields, we predict that there are likely a few hundred more seismically detectable giants in the SCVZ, particularly at brighter G. Assuming the NCVZ has similar statistics, across the north and south the potential seismic CVZ giant sample could be as large as $\sim 10^4$ stars. Based on this model, we predict that seismic detections can be made for $\sim 3 \times 10^5$ giants across the whole sky (i.e. for $N_{\rm sectors} = 1$, subject to the limits on $\nu_{\rm max}$ outlined above (in good agreement with the expectations of Silva Aguirre et al. 2020).

3.3 Constraints on stellar mass and age

Using `PARAM`, we make constraints on mass and age for the set of stars with BHM results that had consistent $\nu_{\rm max}$ and $\Delta\nu$ with the COR and A2Z pipelines, and that had seismic luminosities consistent with those derived from *Gaia* (i.e. `numax_dnu_consistent` = 1 and `lum_flag_BHM` = 1 when using the catalogue presented in Appendix D). The resulting sample has 1749 stars, although we include `PARAM` results in the final catalogue for every target that had BHM results and *SkyMapper*/*TESS*-HERMES parameters that did not meet these criteria (4453 stars). Additionally, we provide `PARAM` results for the 351 of the 513 stars with APOGEE spectra that had robust BHM results, using the APOGEE catalogue stellar parameters as constraints.

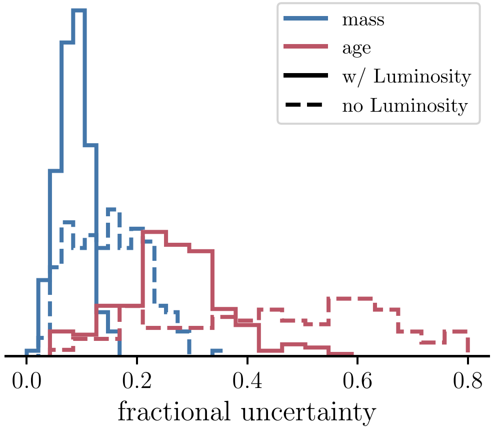

Figure 6. Histograms of fractional formal uncertainties on mass (blue) and age (red) from `PARAM` using *SkyMapper*/*TESS*-HERMES stellar parameters and BHM seismic results. We compare the effect of including *Gaia* luminosity as a constraint between the dashed (no luminosity) and solid (including luminosity) histograms for age and mass. Inclusion of the *Gaia* luminosity improves the median uncertainties from 15 per cent to 8 per cent in mass, and 50 per cent to 26 per cent in age.

Since the seismology results are likely to not yet be optimal, we test how the inclusion of *Gaia* luminosity, $L_{\rm phot.}$, as a constraint for `PARAM` influences the accuracy and precision of our mass and age constraints. The median precision on $\nu_{\rm max}$ and $\Delta\nu$, at a level of 5 per cent and 3 per cent, will not currently provide adequate constraints on mass and age without additional constraints, although individual pipelines report measurements of these parameters at much higher precision. In Fig. 6, we show the distribution of fractional uncertainty in mass and age for the 1749 star sample described above. These uncertainties are 'internal' in the sense that they assume that the grid of stellar models used in `PARAM` are correct in an absolute sense. Dashed histograms show uncertainties when $L_{\rm phot.}$ is not included as a constraint in `PARAM`, whereas the solid histograms show the same when $L_{\rm phot.}$ is included. The uncertainties are clearly tightened up when luminosity constraints are included. Formally, the median uncertainty on mass decreases from 15 per cent to 8 per cent, and on age from 50 per cent to 26 per cent. Without using $L_{\rm phot.}$, the age uncertainties have a large spread, with many stars exceeding 70 per cent uncertainties, whereas its inclusion reduces 93 per cent of the stars to uncertainties of less than 40 per cent. Clearly, improving precision and accuracy on luminosities with better spectroscopic data, for example, will improve our constraints on mass and age. Furthermore, this demonstrates that the *TESS* seismic results are not yet optimal, and can be improved via refinements of the light curves and analyses of them.

For the remainder of the paper, we focus solely on the results that use $L_{\rm phot.}$ as an additional constraint. Furthermore, we include only these results in our final catalogue, as they are likely to be the most robust. We refer to results based on the *SkyMapper*/*TESS*-

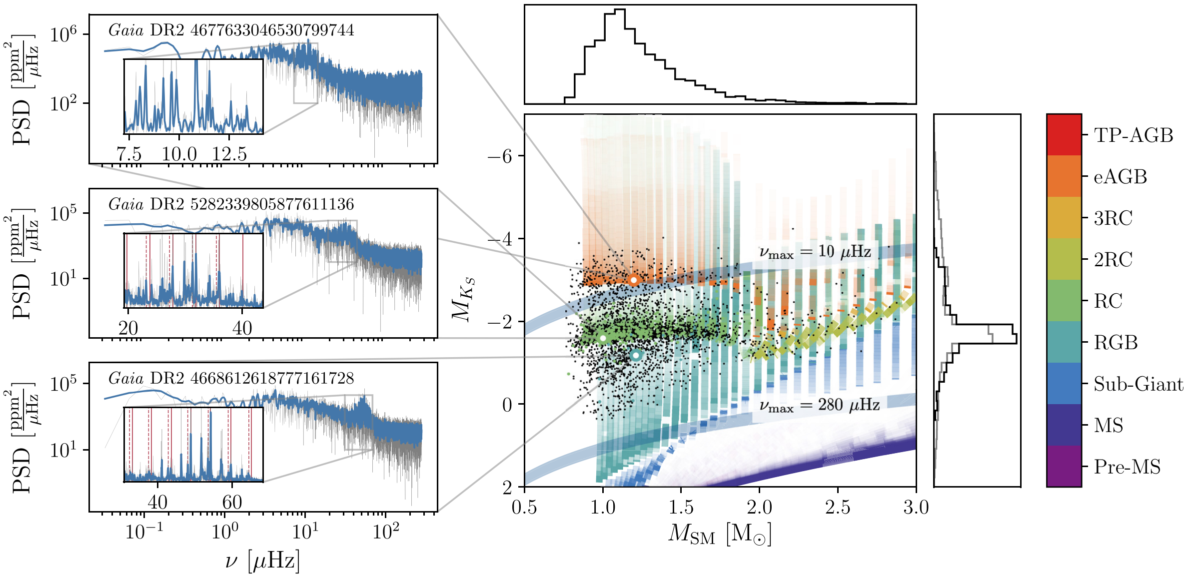

Figure 7. Left: Examples of the seismic detections made by *TESS* across the evolutionary stages of giants in the CVZ. Clear power excess is seen in the log–log space spectra, and oscillation modes are resolved within these envelopes. The $l = 0$ and $l = 2$ modes are shown by the red solid and dashed vertical lines (respectively) in the lower two panels. The top panel shows a candidate AGB bump star, which has a complicated mode structure. Right: Mass against absolute K_S-band magnitude M_{K_S} for CVZ giants with detections in the BHM pipeline (which have a seismic luminosity consistent with that from *Gaia*), compared with a set of solar metallicity isochrones from PARSEC, with the evolutionary stages demonstrated in colour. The RC phase is divided into three stages RC, 2RC, 3RC, which represent the core helium burning phase of low-, intermediate- and high-mass stars, respectively. RC giants whose state is confirmed using the methods of Vrard, Mosser & Samadi (2016) are shown as green scatter points. The histograms demonstrate the marginalized distribution of mass and M_{K_S} (the full underlying distribution of M_{K_S} is shown in grey). The positions of the example stars in this space are indicated by large white points, and the M_{K_S} range at which $\nu_{\rm max}$ is equal to 10 and 280 μHz at each mass (for a representative range in $T_{\rm eff}$) is shown by the labelled blue bands.

HERMES parameters as age$_{\rm SM}$ and $M_{\rm SM}$, and those based on APOGEE spectroscopic constraints as age$_{\rm APO}$ and $M_{\rm APO}$.

3.4 Stellar astrophysics

The potential for *TESS* to provide accurate asteroseismic parameters for many giants on an all-sky basis has been shown for single-sector 27-d data by Silva Aguirre et al. (2020). The year-long data provided by targets in the CVZ in the north and south allow detections of asteroseismic signal at lower frequencies, making the seismic parameters of brighter (and thus larger radii) giants more readily measurable. Longer time series also afford higher frequency resolution, which allow features in the spectra from mixed modes and rotational splitting to be measured (e.g. Mosser et al. 2019). Shorter time series make such analyses more difficult (e.g. Campante et al. 2019). In this section, we demonstrate the prospects for new constraints on models of stellar structure and evolution using asteroseismology of giants in the 13 sectors of data in the CVZ.

Fig. 7 shows examples of power spectra for stars in the *TESS*-SCVZ sample at different evolutionary stages. The right-hand panel shows stellar mass M as estimated using the BHM seismic and SkyMapper/*TESS*-HERMES spectroscopic parameters in `PARAM` against the absolute K_S-band magnitude M_{K_S}, computed using the *Gaia* DR2 parallaxes. The lines plotted underneath show evolutionary tracks from the PARSEC stellar evolution models (Bressan et al. 2012; Marigo et al. 2017). Each line is coloured by the evolutionary stage as provided in the PARSEC tracks and shaded to reflect the relative time spent by a star at each point, emphasizing the phases where an overdensity of stars should be expected. The mass–M_{K_S} distribution of the *TESS*-SCVZ giants roughly matches the prediction of the PARSEC tracks, with the RC clearly visible. There is also an overdensity at brighter M_{K_S} than the RC, which corresponds with the asymptotic giant branch (AGB) phase in the PARSEC tracks. Many of these stars are likely to be in the AGB ‘bump’. This feature was originally highlighted in stellar tracks by Caputo, Castellani & Wood (1978), observed in external galaxies by Gallart (1998) and recently characterized in *Kepler* by Bossini et al. (2015).

The left-hand panels of Fig. 7 show the power spectra of the stars indicated in the right-hand panel, which were selected as examples of the main evolutionary stages that are represented in the data. The top panel shows a star with a very low $\nu_{\rm max}$ (<12 μHz), at an M_{K_S} and M_G value consistent with that of AGBb stars. Oscillation modes are clearly present, but have a more complex structure (since they are further from the asymptotic regime, e.g. Stello et al. 2014). This complexity is evident in modelled oscillations of such stars. The luminosity ratio between the RC and the AGBb is of importance in constraining the size of the C–O core at the end of the core-He burning phase, given its weak dependence on the metallicity and initial helium abundance (e.g. Bono et al. 1995). The *TESS*-CVZ bright giant sample provides a largely unbiased sample of these early AGB stars for which detailed seismic inference is possible. The target selection of e.g. *Kepler* was complex and biased against luminous stars (see e.g. Pinsonneault et al. 2014; Girardi et al. 2015; Sharma et al. 2016), while K2 only measures short time series and therefore does not provide the necessary frequency resolution (see e.g. fig. 1 of Stello et al. 2015).

The lower two panels on the left-hand side of Fig. 7 show spectra of exemplar RC and red giant branch (RGB) stars. Again here, oscillation modes are clearly detected in both stars. RGB and RC stars have been examined in detail in previous asteroseismic samples from e.g. CoRoT, *Kepler* and also in *TESS*. For this reason, our prior knowledge of their mode structure is good, facilitating their

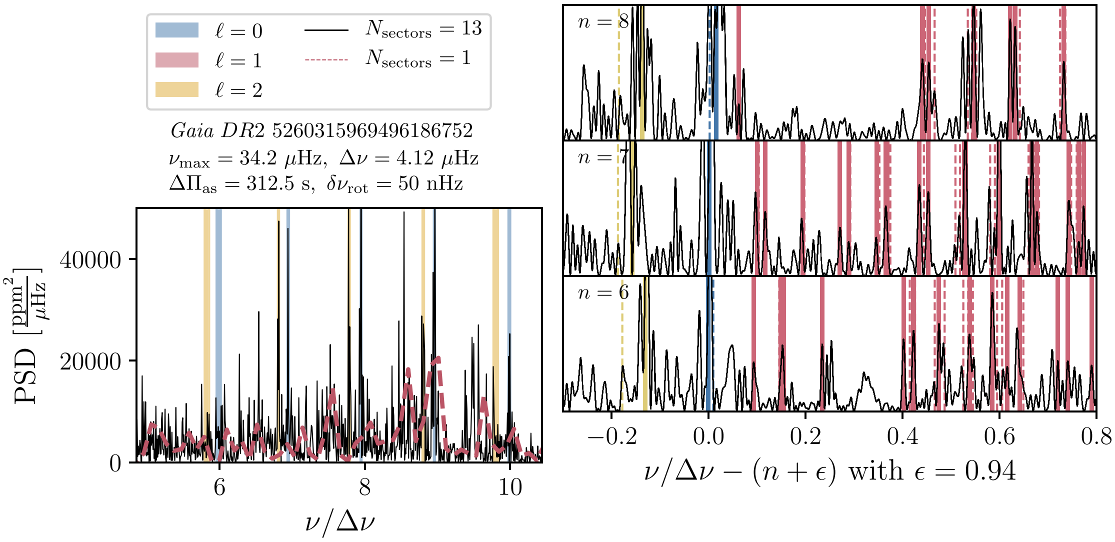

Figure 8. Example of mixed modes visible in an RC giant identified using the period spacing method of Vrard et al. (2016). The spectrum around the power envelope is shown on the left, with zoomed sections at each radial order on the right. The $\ell = 0, 2$ modes (identified with `PBJam`) are indicated by the blue and yellow bands. At each order, a 'forest' of $\ell = 1$ modes is clearly visible, split into a number of separated peaks. The power spectrum of the same star based on 1 sector of data is shown by the red dashed line, demonstrating that these modes would not be detected in that data. A fit to the oscillation modes following the methods of Mosser et al. (2015, 2018) is shown by the dashed and solid vertical lines in the right-hand panel. Solid lines show the observed modes, whereas dashed shows the prediction of the asymptotic relation. Blue and yellow bands indicate $\ell = 0, 2$ modes, as before. Red lines show the positions of the $\ell = 1$ mixed modes detected in the fit, which are split by stellar rotation at a level of $\delta\nu_{\rm rot} = 50$ nHz.

automated detection (peak-bagging) using the `PBJam`[5] code (Nielsen et al. 2021). The $\ell = 0$ and $\ell = 2$ modes are cleanly detected and are shown by the red vertical lines in the inset panels. $\ell = 1$ modes are visible in between the $l = 0$, 2 pairs, with clear evidence of mixed pressure and gravity modes visible within each order. While we do not make use of individual mode measurements in our analysis, this demonstrates that such analyses are inherently possible with *TESS*.

We further demonstrate the ability of the *TESS*-CVZ data to study mixed modes and rotational splitting in red giant stars in Fig. 8. We show the power spectrum around $\nu_{\rm max}$ for an RC giant identified using methods outlined in Vrard et al. (2016). In the left-hand panel, the nearest five radial orders to $\nu_{\rm max}$ are shown. The right-hand panel shows the modes at $n = 6$, 7, 8, and the results of a fit to the $\ell = 0$, 1, and 2 modes following Mosser et al. (2015, 2018). The solid black line shows the power spectrum based on the full 13 sector data set, whereas the underlying dashed red line shows the same generated based on just 27 d (a single sector) of data. In the left-hand panel, we identify the positions of $\ell = 0$, 2 modes as fit by `PBjam` (blue and yellow vertical bands, width indicates 95 per cent confidence interval). The structure between these modes is due to $\ell = 1$ dipole modes. It is evident in the 13 sector curve that these modes divide into multiple separated peaks, whereas such behaviour is not visible in the single sector data (dashed line). In red giant stars, mixed modes are generated by coupling of pressure and gravity modes, which is related to the density contrast between the core and the convective envelope of the star (e.g. Montalbán et al. 2010; Bedding et al. 2011; Beck et al. 2011; Mosser et al. 2012). The fit to the dipole modes in the right-hand panel shows that not only do we detect mixed modes, but also tentatively detect splitting within these modes due to stellar rotation. The best-fitting mean rotational splitting of the mixed modes is $\delta\nu_{\rm rot} = 50$ nHz, with a similar splitting indicated across multiple orders. It is important to note that this value is just above the threshold of $\delta\nu_{\rm rot} \simeq 30$ nHz implied by the frequency resolution. Our detection of rotational splitting in an RC star here is comparable in scale to initial measurements of red giants based on ∼500 d of *Kepler* data (Beck et al. 2012).

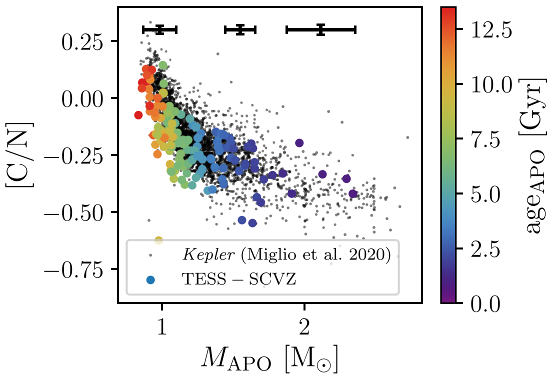

Figure 9. Mass versus the ratio of carbon and nitrogen abundances, [C/N], for the 351 *TESS*-CVZ stars with results from `PARAM` based on APOGEE spectroscopic constraints and BHM seismic results, compared to the same relationship from the study of *Kepler* stars by Miglio et al. (2021) (shown as small black points). The *TESS*-SCVZ points are coloured by the age derived from `PARAM`, and the median uncertainty on mass and [C/N] is demonstrated at three characteristic masses by the black error bars. The *TESS*-SCVZ results broadly follow the same trends as those from *Kepler*.

Finally, in Fig. 9, we demonstrate that the trend between stellar mass and ratio of the photospheric carbon and nitrogen abundances, [C/N], which is readily seen in APOKASC and other data sets (e.g. Masseron & Gilmore 2015; Martig et al. 2016; Silva Aguirre et al. 2020), is also broadly reproduced by our *TESS*-SCVZ results. Here, we use the subset of stars in our sample which have APOGEE spectra, that were re-analysed in PARAM with these tighter spectroscopic

---

[5] https://github.com/grd349/PBjam

constraints. We compare with the data set of (Miglio et al. 2021), which used a very similar analysis to derive stellar mass. The [C/N] has a relationship with mass in giant stars due to the first dredge-up (FDU) of material from the stellar interior as the star evolves away from the main sequence (e.g. Salaris et al. 2015; Lagarde et al. 2017). Burning of hydrogen by the CN and then CNO cycle while on the main sequence produces nitrogen in the stellar core. The convective envelope during the FDU reaches deeper into the interior for more massive stars, which increases the surface [C/N] on the RGB. This effect is clearly seen in the *TESS*-CVZ data.

3.5 Galactic archaeology

Stellar ages are essential, alongside element abundance information and kinematics, to the understanding of the formation and evolution of our Galaxy. As we have shown, *TESS* can provide reliable seismic constraints for $\sim 10^5$ giants in the nearby Milky Way, across the whole sky, and $\sim 10^4$ with at least 1 yr of data. In combination with spectroscopic constraints and modelling, seismic parameters derived from these light curves will provide these essential age constraints. Seismology and stellar modelling presently provides one of the most precise means by which to determine stellar ages (with success already in *TESS*; e.g. Silva Aguirre et al. 2020), and perform detailed studies of the formation and evolution of the Galaxy (e.g. Miglio et al. 2013; Casagrande et al. 2016; Anders et al. 2017a, b; Silva Aguirre et al. 2018; Montalbán et al. 2020; Miglio et al. 2021). These accurate age constraints then provide ideal training sets for data-driven methods of age estimation which can be applied to even larger data sets (e.g. Das & Sanders 2019; Hasselquist et al. 2019; Mackereth et al. 2019; Ciucă et al. 2020). Here, we present a prospective look at the Galactic Archaeology potential of *TESS*.

We first show the kinematics of the sample in Fig. 10. The coloured points show the radial to tangential velocity v_R–v_T (top) and radial to vertical velocity v_R–v_z (bottom) distribution of the sample with robust ages, determined using the BHM seismic constraints and *SkyMapper* parameters, with the colour corresponding to the median age of the posterior distribution from `PARAM`. The contours show the same kinematics for the full underlying sample of *TESS*-CVZ giants. Many of the commonly discussed velocity space substructures at the solar vicinity are visible in the full sample. In particular, the *Hercules* stream/gap (e.g. Dehnen 1998) is visible in the lower left of the distribution of the top panel. A tentative inspection of stars either side of this gap reveals that those at low v_T seem to have slightly older ages. Recent studies of moving groups in age space have shown that there may be important constraints on the disc dynamics to be made based on relative ages such as these (Laporte et al. 2020). Furthermore, the *TESS*-CVZ sample, and larger samples enabled by the use of one-sector *TESS* data or fainter stars will provide new constraints on the local age–velocity dispersion relation (also recently studied in detail by e.g. Ting & Rix 2018; Mackereth et al. 2019; Miglio et al. 2021). In the bottom panel of Fig. 10, the eldest stars clearly have the largest dispersion in v_R and v_z.

In Fig. 11, we demonstrate how even the limited spatial extent of the *TESS*-SCVZ sample still 'dynamically' samples a large part of the Galactic disc. Using the kinematic information from *Gaia* DR2 shown above, we integrate the present-day orbits of each star backwards in `galpy`'s `MWPotential2014` axisymmetric, static potential. For stars with age estimates from `PARAM` (using the BHM pipeline results and *SkyMapper* parameters), we integrate to that age. For stars with no age estimate, we integrate to 2 Gyr ago, which is the typical age of stars for which ages could be determined. In the left-hand panel of Fig. 11, we show the resulting distribution of mean orbital Galactocentric radii $R_{\rm mean}$ as compared to the present-day radial extent (shown by the vertical black lines). The right-hand panels demonstrate the spatial positions in the Galaxy (in an edge-on and face-on view) of the sample after the back-integration, in comparison with the approximate present-day spatial extent of the sample, shown by the black triangles. It is clear that the stars present in the *TESS*-SCVZ are members (in a dynamical sense) of a far more widely distributed population. While this is of course true for any local sample or field, it emphatically demonstrates the richness of the seismic data available.

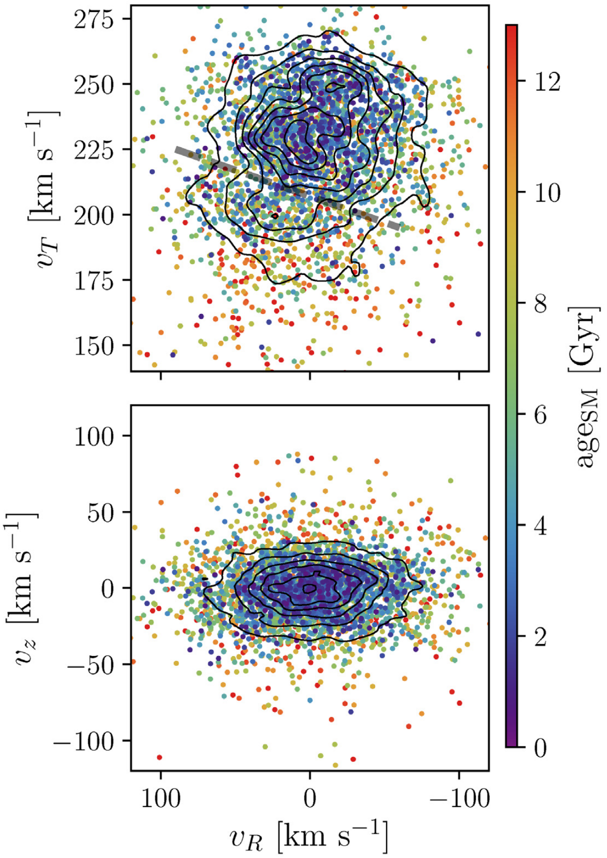

Figure 10. Kinematics of the *TESS*-SCVZ sample with age estimates based on the BHM seismic constraints and *SkyMapper* stellar parameters. The top panel shows the v_R–v_T plane, and the bottom shows v_R–v_z. Points show each star from the sample with reliably measured ages, coloured by the age estimate from `PARAM`, plotted in reverse order, such that the youngest stars appear in the foreground. The contours demonstrate the kinematics of the full underlying sample. The commonly discussed velocity substructures in the disc (e.g. the *Hercules* stream/gap feature at $v_R < 0\,{\rm km\,s^{-1}}$, $v_T < 210\,{\rm km\,s^{-1}}$) are visible in the underlying sample, and we indicate this in the top panel by the thick dashed line. The stars for which we have measured ages appear to sample these features well.

Fig. 12 shows the trends between the stellar mass (which is determined more precisely than the age in most cases) and the mean orbital radius $r_{\rm mean}$ and maximum vertical excursion from the mid-plane $z_{\rm max}$. At increased stellar mass (and therefore younger ages on average), the width of the $r_{\rm mean}$ distribution decreases markedly, such that the lowest mass stars have orbits whose mean radii cover the largest extent of the disc. This is a clear signal of radial mixing of disc stars, and has been noted in a number of studies (e.g. Casagrande et al. 2011; Frankel et al. 2018, 2019, 2020; Sharma, Hayden &

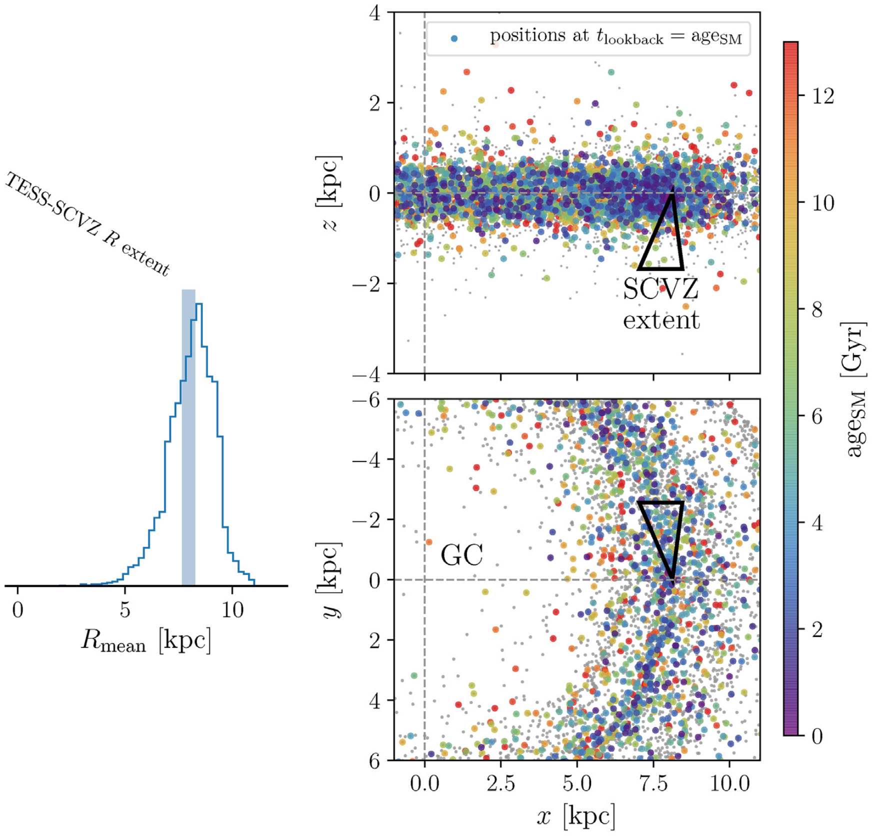

Figure 11. The spatial extent of the *TESS*-SCVZ sample compared with the extent which is 'dynamically' sampled by the data. The histogram on the left compares the extent in Galactocentric R today (blue shaded region) with the distribution of mean orbital radii R_{mean} in the sample (blue histogram). The right-hand panels show the spatial distribution in Galactocentric Cartesian coordinates when the sample is integrated backwards to its apparent age (coloured points) or 2 Gyr for stars with no age estimates (small black points) in an axisymmetric potential. The approximate extent today of the SCVZ sample is shown by the black triangles.

Bland-Hawthorn 2020; Miglio et al. 2021). Similarly, at lower mass, stars have a wider distribution in z_{max}, a clear example of dynamical heating of the disc (e.g. Aumer, Binney & Schönrich 2016; Ting & Rix 2018; Mackereth et al. 2019). The measurement of precise ages for nearby stellar samples provides an ideal data set for testing models of radial mixing and dynamical heating processes.

Further, Fig. 13 demonstrates the relationship between age, element abundances, and kinematics of the *TESS*-SCVZ sample with APOGEE DR16 spectra (513 stars). The top panel shows the [Fe/H]–[Mg/Fe] plane (which has been studied extensively in a Galactic Archaeology context; e.g. Haywood et al. 2013; Nidever et al. 2014; Hayden et al. 2015; Queiroz et al. 2020) coloured by the stellar age (based on analysis using the more precise APOGEE DR16 stellar parameters). The high [Mg/Fe] stars that separate from the solar [Mg/Fe] population at [Fe/H] $\lesssim 0.2$ are clearly separate in age, and are generally older than ∼10 Gyr (aside from some notable outliers, see below). The solar [Mg/Fe] population has a wider spread in ages below ∼10 Gyr, and a relatively clear trend towards younger age with decreasing [Mg/Fe]. These trends are also broadly seen in other studies of the [Fe/H]−[Mg/Fe] plane with stellar ages (or their proxies; e.g. Haywood et al. 2013; Anders et al. 2017a; Hasselquist et al. 2019; Mackereth et al. 2019).

This trend is much clearer in the lower right panel, which shows [Mg/Fe] as a function of age, now coloured by the mean orbital radius for each star. As age increases from ∼0 to ∼10 Gyr, the mean [Mg/Fe] increases by almost 0.1 dex. Stars older than ∼10 Gyr have a larger spread in [Mg/Fe] and are those corresponding to the high [Mg/Fe] track in the upper panel. The R_{mean} of these stars indicates that they are likely to be members of populations formed in the inner disc of the Galaxy which have eccentric orbits and thus have travelled to the solar radius.

The mean orbital radii also indicate useful information in the lower left panel, showing [Fe/H] as a function of age, again coloured by R_{mean}. At intermediate age (∼3–8 Gyr) and, to a lesser extent outside of this range, there is a large spread in [Fe/H] at fixed age. Stars with high R_{mean} tend to be young and have lower [Fe/H]. The most metal-rich stars are old and have lower R_{mean}. This gradient in R_{mean} across the range in [Fe/H] is to be expected given that the Milky Way disc has a shallow, yet significant, metallicity gradient (e.g. Cheng et al. 2012; Bergemann et al. 2014; Anders et al. 2017b). The lack of a clear relationship between age and [Fe/H] is likely a manifestation of radial migration in the disc, and has been discussed at length in the literature (Sellwood & Binney 2002; Minchev et al. 2012; Solway, Sellwood & Schönrich 2012; Minchev, Chiappini & Martig 2013; Vera-Ciro et al. 2014; Grand, Kawata & Cropper 2015; Frankel et al. 2018, 2020).

Finally, we show the age distributions of our samples in Fig. 14. We divide the APOGEE-based ages into high and low [Mg/Fe] groups, using the visually determined division shown in the top panel of Fig. 13. We estimate the posterior distribution of the observed ages using a Gaussian kernel density estimation applied to 1000 samples from the posterior on each star from `PARAM`. The *SkyMapper* and

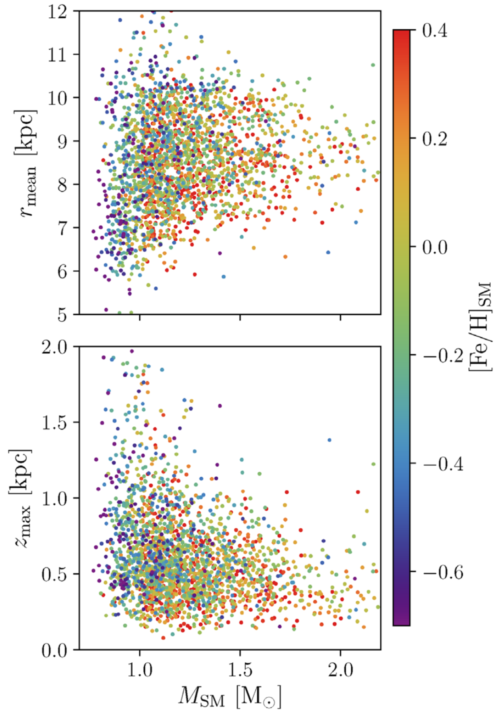

Figure 12. The stellar mass as estimated using `PARAM` applied to the BHM pipeline and *SkyMapper* parameters, against the mean orbital radius $r_{\rm mean}$ and the maximum vertical excursion above the plane $z_{\rm max}$. The colour of the points is determined by the [Fe/H] from *SkyMapper*. It is clear that the lowest mass (and therefore oldest, on average) stars are those whose orbits cover the greatest radial and vertical extents. There is a clear relationship with [Fe/H], such that at higher mass (and thus younger ages), stars are generally more metal rich.

low [Mg/Fe] APOGEE ages have qualitatively similar distributions, suggesting that the *SkyMapper* sample is dominated by low [Mg/Fe] stars. The high [Mg/Fe] stars have a bimodal age distribution, with a strong peak at ∼10 Gyr. This peak is consistent with the old age for the high [α/Fe] disc as shown by a number of studies (e.g. Fuhrmann 2011; Haywood et al. 2013; Silva Aguirre et al. 2018; Miglio et al. 2021). The young peak is likely to be a result of ‘overmassive’, apparently ‘young’ α-rich stars, contaminating the sample (Chiappini et al. 2015; Martig et al. 2015; Jofré et al. 2016; Hekker & Johnson 2019). These stars are outliers to the true age distribution of the high [α/Fe] disc. Evidence collected thus far strongly suggests that these are stars that have undergone some mass transfer with a (now unseen) companion earlier in their lives and thus appear young to asteroseismic methods (see discussion in, e.g. Miglio et al. 2021). Each sample has a long tail extending to high ages driven by the uncertainties on individual ages, which are Gaussian in $\log_{10}$(age), due to the prior adopted in `PARAM`.

We fit a mixture model for the intrinsic age distribution of the high [Mg/Fe] stars, following the methodology of Miglio et al. (2021). This model accounts for the contamination by ‘overmassive’ stars, and recovers the intrinsic spread in age of the population (i.e. other than that caused by the age uncertainties). We find results that are consistent with those of Miglio et al. (2021): the mean age of the population is $\mu = 11.3 \pm 0.8$ Gyr, with an intrinsic spread (defined as the standard deviation in linear age) of $\delta_{\rm age} = 1.3^{+0.6}_{-0.8}$ Gyr. The best-fitting model and the 1σ uncertainty are shown by the dashed grey line and band in Fig. 14. It is clear that the age uncertainties inflate the distribution considerably, but careful modelling accounting for these uncertainties can recover the underlying age spread. This demonstrates that it will still be possible to make important inferences of, for example, the Galactic star formation history using *TESS* ages, despite the relatively lower asteroseismic precision (relative to, e.g. *Kepler*) afforded by the data.

Finally, we note that our mixture model finds a contamination of the high [Mg/Fe] stars by ‘overmassive’ stars at a level of 15^{+11}_{-7} per cent. This contamination is a little higher but not inconsistent above the 1σ level, than the results of Miglio et al. (2021). It is likely that the differences in selection between these two works likely brings about some population bias that may affect these numbers. Future studies that aim to determine the origin and nature of these ‘overmassive’ stars will need to account for these biases.

4 SUMMARY AND CONCLUSIONS

We have demonstrated the strong potential for Galactic archaeology and stellar astrophysics, and asteroseismic quality of year-long photometry from the *TESS*-CVZ. Studying a sample of 15 405 giants in- and outside the CVZ, we demonstrate that currently achieved seismic yields are comparable or better to those estimated using a model of detection probability in *TESS* and produce precise stellar ages, masses, and radii when combined with spectroscopic constraints. Power spectra derived from the time series data provide clear detections of oscillation modes in stars in a large range of evolutionary states, providing great potential for new constraints on stellar evolution models. To summarize our findings as follows:

(i) **Systematics:** A number of systematics are evident in the light curves that we generate based on the *TESS* FFI, which appear worsened in the 1 yr data. More detailed correction of these will be required to ascertain the best possible seismic data. It is likely that many such issues can be resolved with some extra treatment of our light curves.

(ii) **Seismic detection yields:** We find that the realized detection yields from the *TESS*-CVZ compare well with a simple model for the detection probability, but only after accounting for dilution effects. After confirming seismic detections using luminosities derived with 2MASS and *Gaia* for 8249 stars, we find an average detection yield of ∼36 per cent (2890 stars), which increases to ∼50 per cent when stars with a year of data are considered. We presently suffer from issues in procuring seismic parameters for brighter stars with $\nu_{\rm max} < 10\,\mu$Hz, which likely will require specifically tuned analysis methods.

(iii) **Constraints on stellar mass and age:** We produce mass and age constraints for 1749 stars, based on *SkyMapper*/*TESS*-HERMES stellar parameters and BHM seismic parameters using the `PARAM` Bayesian parameter estimation code. By comparing the uncertainties on mass and age when *Gaia* luminosities are used as constraints or not, we show that without refining the current seismic parameter measurements, an external luminosity constraint is required to achieve adequate precision (i.e. less than 10 per cent in mass and 30 per cent in age) on these parameters.

(iv) **Seismology across the Hertzsprung–Russell diagram:** The *TESS*-CVZ data provide good power spectral resolution even for relatively low $\nu_{\rm max}$ stars. We show that stars on the AGB bump are clearly detected in our sample, and the detection of mixed modes and, tentatively, rotational splitting is possible in RC stars with 12 sectors of data. Importantly, target selection effects are more simply accounted for in the *TESS*-FFI samples than in, for example, *Kepler*.

(v) **Galactic archaeology in the Milky Way disc:** The *TESS*-SCVZ sample provides a good sampling of velocity space in the

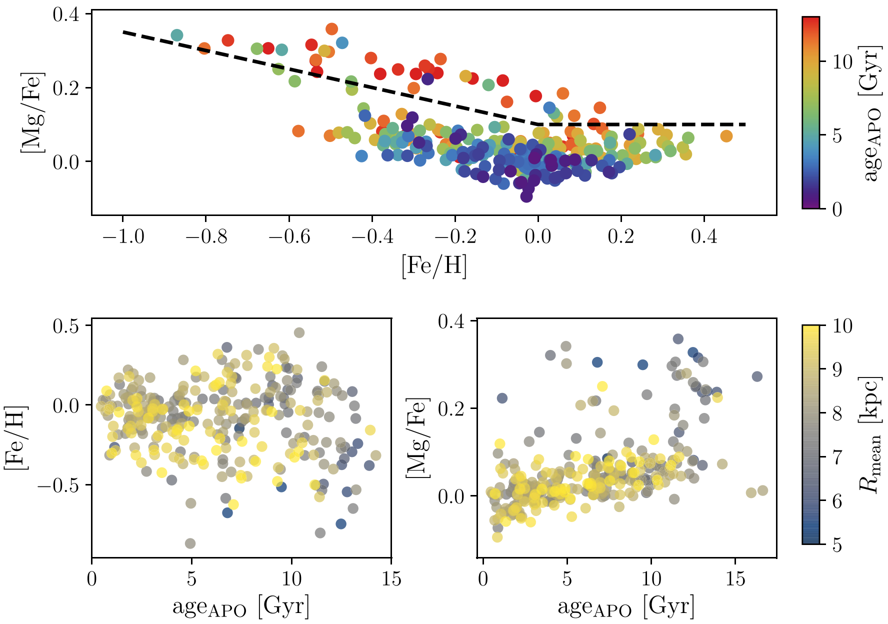

Figure 13. [Mg/Fe], [Fe/H], and age for the 351 *TESS*-CVZ bright giants that have detailed abundances from APOGEE-DR16 and results from `PARAM` based on the BHM seismic parameters. The upper panel shows the [Mg/Fe]–[Fe/H] plane coloured by stellar age. The dashed line indicates the visually defined separation which we make between high and low [α/Fe] stars. The lower panels show each of these abundance ratios as a function of stellar age, and colour indicates there the mean orbital radius $R_{\rm mean}$ of each star. There is a clear dichotomy in age between the old, high [Mg/Fe] stars and the younger, low [Mg/Fe] stars. Similarly, the older populations have markedly lower mean radii and are on excursions from the inner regions of the disc.

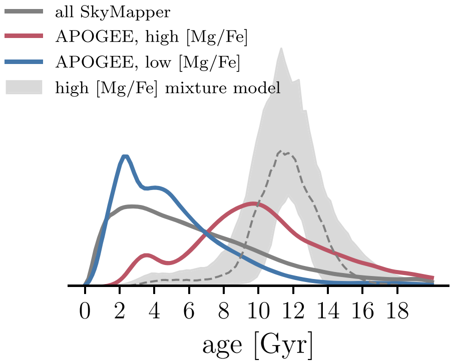

Figure 14. The posterior distributions of observed ages for high and low [Mg/Fe] stars in common with APOGEE (shown by the red and blue curves, respectively), and the full sample in common with *SkyMapper* (in grey). We estimate the posterior using a Gaussian kernel density estimation applied to samples from the individual age posteriors from `PARAM`. The mixture model for the intrinsic age distribution of high [Mg/Fe] stars and its 1σ uncertainty is shown by the grey dashed line and band. Despite the relatively large age uncertainties, the mixture model recovers the intrinsic age distribution for high [Mg/Fe] stars found by previous works.

solar vicinity. Trends between stellar mass (and therefore age) and the mean radii and maximum vertical excursions of stellar orbits are clearly visible. By integrating the orbits of stars in our sample, we demonstrate that the data from the CVZ, although limited in spatial extent, ‘dynamically’ samples a large section of the Milky Way disc with 5 kpc $\lesssim R \lesssim$ 10 kpc. The age precision afforded by *TESS*, in combination with high-resolution spectroscopic data from APOGEE, is enough to distinguish clear differences in age between the high and low [Mg/Fe] disc stars and will be of great utility in properly reconstructing the star formation history of the disc.

In particular, this paper has demonstrated the great importance of spectroscopic follow up for giants in the *TESS*-CVZs. We predict that seismic samples of the order of a few 10^4 giants could be attainable in the CVZs, but age and mass estimates will only be readily available – and sufficiently precise – for stars that also have spectroscopic information. Such spectroscopic data will likely become available from future survey data (e.g. GALAH: Martell et al. 2017; SDSS-V: Kollmeier et al. 2019), but high-resolution, high-SNR samples may be of great utility to the community as calibration data.

Careful modelling of large samples of asteroseismic data will afford detailed insights into the formation and evolution in the disc. Furthermore, it is likely possible to further pin down the precision on these stellar ages, using novel analysis techniques based on machine learning (Hon, Stello & Yu 2018; Ness et al. 2018; Blancato et al. 2020) or more detailed modelling (and fitting) of the power spectra (e.g. Rendle et al. 2019; Montalbán et al. 2020). In addition to this, it is foreseeable that samples from the CVZs will be useful as training data for future data-driven analyses, providing time series with consistent noise statistics but longer baselines than the whole-sky *TESS* data.

ACKNOWLEDGEMENTS

JTM and AM acknowledge support from the ERC Consolidator Grant funding scheme (project ASTEROCHRONOMETRY, G.A. n. 772293). JTM acknowledges support from the Banting Postdoctoral Fellowship programme administered by the Government of Canada, and a CITA/Dunlap Institute fellowship. The Dunlap Institute is funded through an endowment established by the David Dunlap family and the University of Toronto. SM acknowledges support from the Spanish Ministry with the Ramon y Cajal fellowship number RYC-2015-17697. RAG acknowledges the support from the PLATO CNES grant. DB acknowledges supported by FCT through the research grants UIDB/04434/2020, UIDP/04434/2020, and PTDC/FIS-AST/30389/2017, and by FEDER – Fundo Europeu de Desenvolvimento Regional through COMPETE2020 – Programa Operacional Competitividade e Internacionalização (grant: POCI-01-0145-FEDER-030389). LC acknowledges support from the Australian Research Council grant FT160100402. TC acknowledges support from the European Union's Horizon 2020 research and innovation programme under the Marie Skłodowska-Curie grant agreement no. 792848 (PULSATION). AS is partially supported by grants ESP2017-82674-R (Spanish Government) and 2017-SGR-1131 (Generalitat de Catalunya). MHP and MV acknowledge support from NASA grant 80NSSC18K1582.

This paper includes data collected by the *TESS* mission. Funding for the *TESS* mission is provided by the NASA Explorer Program.

This work has made use of data from the European Space Agency (ESA) mission *Gaia* (https://www.cosmos.esa.int/gaia), processed by the *Gaia* Data Processing and Analysis Consortium (DPAC, https://www.cosmos.esa.int/web/gaia/dpac/consortium). Funding for the DPAC has been provided by national institutions, in particular the institutions participating in the *Gaia* Multilateral Agreement.

Funding for the Sloan Digital Sky Survey IV has been provided by the Alfred P. Sloan Foundation, the U.S. Department of Energy Office of Science, and the Participating Institutions. SDSS-IV acknowledges support and resources from the Center for High-Performance Computing at the University of Utah. The SDSS web site is www.sdss.org. SDSS-IV is managed by the Astrophysical Research Consortium for the Participating Institutions of the SDSS Collaboration including the Brazilian Participation Group, the Carnegie Institution for Science, Carnegie Mellon University, the Chilean Participation Group, the French Participation Group, Harvard-Smithsonian Center for Astrophysics, Instituto de Astrofísica de Canarias, The Johns Hopkins University, Kavli Institute for the Physics and Mathematics of the Universe (IPMU)/University of Tokyo, Lawrence Berkeley National Laboratory, Leibniz Institut für Astrophysik Potsdam (AIP), Max-Planck-Institut für Astronomie (MPIA Heidelberg), Max-Planck-Institut für Astrophysik (MPA Garching), Max-Planck-Institut für Extraterrestrische Physik (MPE), National Astronomical Observatories of China, New Mexico State University, New York University, University of Notre Dame, Observatário Nacional/MCTI, The Ohio State University, Pennsylvania State University, Shanghai Astronomical Observatory, United Kingdom Participation Group, Universidad Nacional Autónoma de México, University of Arizona, University of Colorado Boulder, University of Oxford, University of Portsmouth, University of Utah, University of Virginia, University of Washington, University of Wisconsin, Vanderbilt University, and Yale University.

This research made use of MATPLOTLIB, a PYTHON library for publication quality graphics (Hunter 2007), NUMPY (Van Der Walt, Colbert & Varoquaux 2011), SCIPY (Virtanen et al. 2020), the IPYTHON package (Pérez & Granger 2007), SCIKIT-LEARN (Pedregosa et al. 2011), ASTROPY, a community-developed core PYTHON package for Astronomy (Astropy Collaboration 2013, 2018), LIGHTKURVE, a PYTHON package for Kepler and *TESS* data analysis (Lightkurve Collaboration 2018), and Astroquery (Ginsburg et al. 2019).

DATA AVAILABILITY

The processed data underlying this article are available in the article and in its online supplementary material. The raw data (e.g. unprocessed light curves and original data tables) can be made available on reasonable request to the corresponding author.

REFERENCES

Aerts C., 2019, preprint (arXiv:1912.12300)
Ahumada R. et al., 2019, preprint (arXiv:1912.02905)
Anders F. et al., 2017a, A&A, 597, A30
Anders F. et al., 2017b, A&A, 600, A70
Astropy Collaboration, 2013, A&A, 558, A33
Astropy Collaboration, 2018, AJ, 156, 123
Aumer M., Binney J., Schönrich R., 2016, MNRAS, 462, 1697
Auvergne M. et al., 2009, A&A, 506, 411
Baglin A. et al., 2006, in 36th COSPAR Scientific Assembly. p. 3749
Beck P. G. et al., 2011, Science, 332, 205
Beck P. G. et al., 2012, Nature, 481, 55
Bedding T. R. et al., 2011, Nature, 471, 608
Bennett M., Bovy J., 2018, MNRAS, 482, 1417
Bergemann M. et al., 2014, A&A, 565, A89
Blancato K., Ness M., Huber D., Lu Y., Angus R., 2020, preprint (arXiv:2005.09682)
Bono G., Castellani V., degl'Innocenti S., Pulone L., 1995, A&A, 297, 115
Borucki W. J. et al., 2010, Science, 327, 977
Bossini D. et al., 2015, MNRAS, 453, 2290
Boubert D., Everall A., 2020, MNRAS, 497, 4246
Bovy J., 2015, ApJS, 216, 29
Bovy J., Rix H.-W., Green G. M., Schlafly E. F., Finkbeiner D. P., 2016, ApJ, 818, 130
Bowen I. S., Vaughan A. H., 1973, Appl. Opt., 12, 1430
Bressan A., Marigo P., Girardi L., Salasnich B., Dal Cero C., Rubele S., Nanni A., 2012, MNRAS, 427, 127
Brogaard K. et al., 2018, MNRAS, 476, 3729
Campante T. L. et al., 2016, ApJ, 830, 138
Campante T. L. et al., 2019, ApJ, 885, 31
Caputo F., Castellani V., Wood P. R., 1978, MNRAS, 184, 377
Casagrande L., VandenBerg D. A., 2014, MNRAS, 444, 392
Casagrande L., Schönrich R., Asplund M., Cassisi S., Ramírez I., Meléndez J., Bensby T., Feltzing S., 2011, A&A, 530, A138
Casagrande L. et al., 2016, MNRAS, 455, 987
Casagrande L., Wolf C., Mackey A. D., Nordland er T., Yong D., Bessell M., 2019, MNRAS, 482, 2770
Chan V. C., Bovy J., 2020, MNRAS, 493, 4367
Chanamé J., Ramírez I., 2012, ApJ, 746, 102
Chaplin W. J., Miglio A., 2013, ARA&A, 51, 353
Chaplin W. J. et al., 2011, ApJ, 732, 54
Chaplin W. J. et al., 2020, Nat. Astron., 4, 382
Cheng J. Y. et al., 2012, ApJ, 746, 149
Chiappini C. et al., 2015, A&A, 576, L12
Ciucă I., Kawata D., Miglio A., Davies G. R., Grand R. J. J., 2020, preprint (arXiv:2003.03316)
Corsaro E., Fröhlich H. E., Bonanno A., Huber D., Bedding T. R., Benomar O., De Ridder J., Stello D., 2013, MNRAS, 430, 2313
da Silva L. et al., 2006, A&A, 458, 609
Das P., Sanders J. L., 2019, MNRAS, 484, 294
Dehnen W., 1998, AJ, 115, 2384
Drimmel R., Cabrera-Lavers A., López-Corredoira M., 2003, A&A, 409, 205
Elsworth Y., Themeßl N., Hekker S., Chaplin W., 2020, Res Notes Am. Astron. Soc., 4, 177
Fausnaugh M. M., Burke C. J., Caldwell D., Jenkins J. M. et al., 2018, TESS Data Release Notes. NASA
Foreman-Mackey D., Hogg D. W., Lang D., Goodman J., 2013, PASP, 125, 306
Frankel N., Rix H.-W., Ting Y.-S., Ness M., Hogg D. W., 2018, ApJ, 865, 96
Frankel N., Sanders J., Rix H.-W., Ting Y.-S., Ness M., 2019, ApJ, 884, 99
Frankel N., Sanders J., Ting Y.-S., Rix H.-W., 2020, ApJ, 896, 15
Fuhrmann K., 2011, MNRAS, 414, 2893
Gaia Collaboration, 2018, A&A, 616, A1

Gallart C., 1998, ApJ, 495, L43

García R. A. et al., 2011, MNRAS, 414, L6

García Pérez A. E. et al., 2016, AJ, 151, 144

Ginsburg A. et al., 2019, AJ, 157, 98

Girardi L., Barbieri M., Miglio A., Bossini D., Bressan A., Marigo P., Rodrigues T. S., 2015, in Eggenberger P., Montalban J., eds, Astrophysics and Space Science Proceedings, Vol. 39, Asteroseismology of Stellar Populations in the Milky Way. Springer International Publ., Switzerland, p. 125

Godoy-Rivera D., Chanamé J., 2018, MNRAS, 479, 4440

Grand R. J. J., Kawata D., Cropper M., 2015, MNRAS, 447, 4018

Gravity Collaboration, 2018, A&A, 615, L15

Green G. M., Schlafly E., Zucker C., Speagle J. S., Finkbeiner D., 2019, ApJ, 887, 93

Hall O. J. et al., 2019, MNRAS, 486, 3569

Handberg R., Brogaard K., Miglio A., Bossini D., Elsworth Y., Slumstrup D., Davies G. R., Chaplin W. J., 2017, MNRAS, 472, 979

Hasselquist S. et al., 2019, ApJ, 871, 181

Hayden M. R. et al., 2015, ApJ, 808, 132

Haywood M., Di Matteo P., Lehnert M. D., Katz D., Gómez A., 2013, A&A, 560, A109

Hekker S., Johnson J. A., 2019, MNRAS, 487, 4343

Hogg D. W., Bovy J., Lang D., 2010, preprint (arXiv:1008.4686)

Hon M., Stello D., Yu J., 2018, MNRAS, 476, 3233

Howell S. B. et al., 2014, PASP, 126, 398

Huber D. et al., 2019, AJ, 157, 245

Hunter J. D., 2007, Comput. Sci. Eng., 9, 90

Indebetouw R. et al., 2005, ApJ, 619, 931

Jofré P. et al., 2016, A&A, 595, A60

Jönsson H. et al., 2020, AJ, 160, 120

Khan S. et al., 2019, A&A, 628, A35

Kjeldsen H., Bedding T. R., 1995, A&A, 293, 87

Kollmeier J. et al., 2019, in BAAS. p. 274

Lagarde N., Robin A. C., Reylé C., Nasello G., 2017, A&A, 601, A27

Laporte C. F. P., Famaey B., Monari G., Hill V., Wegg C., Gerhard O., 2020, A&A, 643, L3

Leung H. W., Bovy J., 2019, MNRAS, 489, 2079

Lightkurve Collaboration, 2018, Astrophysics Source Code Library, record ascl:1812.013

Lindegren L. et al., 2018, A&A, 616, A2

Luri X. et al., 2018, A&A, 616, A9

Mackereth J. T., Bovy J., 2018, PASP, 130, 114501

Mackereth J. T. et al., 2019, MNRAS, 489, 176

Majewski S. R. et al., 2017, AJ, 154, 94

Manchon L., Belkacem K., Samadi R., Sonoi T., Marques J. P. C., Ludwig H. G., Caffau E., 2018, A&A, 620, A107

Marigo P. et al., 2017, ApJ, 835, 77

Marshall D. J., Robin A. C., Reylé C., Schultheis M., Picaud S., 2006, A&A, 453, 635

Martell S. L. et al., 2017, MNRAS, 465, 3203

Martig M. et al., 2015, MNRAS, 451, 2230

Martig M. et al., 2016, MNRAS, 456, 3655

Masseron T., Gilmore G., 2015, MNRAS, 453, 1855

Mathur S. et al., 2010, A&A, 511, A46

Miglio A. et al., 2013, MNRAS, 429, 423

Miglio A., Chaplin W. J., Farmer R., Kolb U., Girardi L., Elsworth Y., Appourchaux T., Hand berg R., 2014, ApJ, 784, L3

Miglio A. et al., 2016, MNRAS, 461, 760

Miglio A. et al., 2021, A&A, 645, A85

Minchev I., Famaey B., Quillen A. C., Di Matteo P., Combes F., Vlajić M., Erwin P., Bland-Hawthorn J., 2012, A&A, 548, A126

Minchev I., Chiappini C., Martig M., 2013, A&A, 558, A9

Montalbán J. et al., 2020, preprint (arXiv:2006.01783)

Montalbán J., Miglio A., Noels A., Scuflaire R., Ventura P., 2010, ApJ, 721, L182

Mosser B., Appourchaux T., 2009, A&A, 508, 877

Mosser B. et al., 2012, A&A, 540, A143

Mosser B., Vrard M., Belkacem K., Deheuvels S., Goupil M. J., 2015, A&A, 584, A50

Mosser B., Gehan C., Belkacem K., Samadi R., Michel E., Goupil M. J., 2018, A&A, 618, A109

Mosser B., Michel E., Samadi R., Miglio A., Davies G. R., Girardi L., Goupil M. J., 2019, A&A, 622, A76

Nardiello D. et al., 2015, MNRAS, 447, 3536

Nardiello D., Libralato M., Bedin L. R., Piotto G., Ochner P., Cunial A., Borsato L., Granata V., 2016, MNRAS, 455, 2337

Nardiello D. et al., 2019, MNRAS, 490, 3806

Nardiello D. et al., 2020, MNRAS, 495, 4924

Ness M., Hogg D. W., Rix H. W., Martig M., Pinsonneault M. H., Ho A. Y. Q., 2016, ApJ, 823, 114

Ness M. K., Silva Aguirre V., Lund M. N., Cantiello M., Foreman-Mackey D., Hogg D. W., Angus R., 2018, ApJ, 866, 15

Nidever D. L. et al., 2014, ApJ, 796, 38

Nidever D. L. et al., 2015, AJ, 150, 173

Nielsen M. B., et al., 2021, AJ, 161, 62

Onken C. A. et al., 2019, Publ. Astron. Soc. Aust., 36, e033

Pedregosa F. et al., 2011, J. Mach. Learn. Res., 12, 2825

Pérez F., Granger B. E., 2007, Comput. Sci. Eng., 9, 21

Pinsonneault M. H. et al., 2014, ApJS, 215, 19

Pinsonneault M. H. et al., 2018, ApJS, 239, 32

Queiroz A. B. A. et al., 2020, preprint (arXiv:2007.12915)

Rendle B. M. et al., 2019, MNRAS, 484, 771

Ricker G. R. et al., 2015, J. Astron. Telesc. Instrum. Syst., 1, 014003

Rodrigues T. S. et al., 2014, MNRAS, 445, 2758

Rodrigues T. S. et al., 2017, MNRAS, 467, 1433

Salaris M., Pietrinferni A., Piersimoni A. M., Cassisi S., 2015, A&A, 583, A87

Samadi R., Belkacem K., Dupret M. A., Ludwig H. G., Baudin F., Caffau E., Goupil M. J., Barban C., 2012, A&A, 543, A120

Schofield M. et al., 2019, ApJS, 241, 12

Schönrich R., Binney J., Dehnen W., 2010, MNRAS, 403, 1829

Schönrich R., McMillan P., Eyer L., 2019, MNRAS, 487, 3568

Sellwood J. A., Binney J. J., 2002, MNRAS, 336, 785

Sharma S., Bland-Hawthorn J., Johnston K. V., Binney J., 2011, ApJ, 730, 3

Sharma S., Stello D., Bland-Hawthorn J., Huber D., Bedding T. R., 2016, ApJ, 822, 15

Sharma S. et al., 2018, MNRAS, 473, 2004

Sharma S., Hayden M. R., Bland-Hawthorn J., 2020, preprint (arXiv:2005.03646)

Shetrone M. et al., 2015, ApJS, 221, 24

Silva Aguirre V. et al., 2018, MNRAS, 475, 5487

Silva Aguirre V. et al., 2020, ApJ, 889, L34

Skrutskie M. F. et al., 2006, AJ, 131, 1163

Solway M., Sellwood J. A., Schönrich R., 2012, MNRAS, 422, 1363

Stello D. et al., 2014, ApJ, 788, L10

Stello D. et al., 2015, ApJ, 809, L3

Sullivan P. W. et al., 2015, ApJ, 809, 77

Thomas A., Stevenson E., Gittins F. W. R., Miglio A., Davies G., Girardi L., Campante T. L., Schofield M., 2017, EPJ Web Conf., 160, 05006

Ting Y.-S., Rix H.-W., 2019, ApJ, 878, 21

Van Der Walt S., Colbert S. C., Varoquaux G., 2011, Comput. Sci. Eng., 13, 22

Vera-Ciro C., D’Onghia E., Navarro J., Abadi M., 2014, ApJ, 794, 173

Virtanen P. et al., 2020, Nat. Methods, 17, 261

Vrard M., Mosser B., Samadi R., 2016, A&A, 588, A87

White T. R. et al., 2017, MNRAS, 471, 2882

Wilson J. C. et al., 2019, PASP, 131, 055001

Wolf C. et al., 2018, Publ. Astron. Soc. Aust., 35, e010

Yu J., Huber D., Bedding T. R., Stello D., Hon M., Murphy S. J., Khanna S., 2018, ApJS, 236, 42

Zinn J. C., Pinsonneault M. H., Huber D., Stello D., 2019, ApJ, 878, 136

SUPPORTING INFORMATION

Supplementary data are available at *MNRAS* online.

TESS_CVZ_brightgiants_reduced_241120.dat

Please note: Oxford University Press is not responsible for the content or functionality of any supporting materials supplied by the authors. Any queries (other than missing material) should be directed to the corresponding author for the article.

APPENDIX A: SURFACE GRAVITY CONSTRAINTS FOR STARS WITH MISSING DATA

For the best possible constraints on stellar mass and age using a method such as `PARAM`, we require as many constraints on other fundamental stellar parameters as possible. At present, the TESS-SCVZ data are lacking in publicly available spectroscopic follow-up, and so these stellar parameters must be gathered by alternative means. As described above, we use a combination of data from *SkyMapper*, *TESS*-HERMES, and APOGEE. There are a number of stars for which an estimate of log(g) is not available from *TESS*-HERMES. Here, we exploit the fact that there is a correlation between $T_{\rm eff}$ and luminosity L, which in turn correlates with R and thus the surface gravity log(g) with some dependence on [Fe/H], to constrain a prior on log (g) for stars that have $T_{\rm eff}$ and [Fe/H].

We use a simple method to infer log(g) for those stars that only had photometric $T_{\rm eff}$ and [Fe/H] from *SkyMapper*. Using the 1186 stars in our sample for which spectroscopic log (g) *was* available from *TESS*-HERMES, we construct a Gaussian KDE of log(g), $T_{\rm eff}$, and [Fe/H] space, adopting a kernel with a bandwidth determined via Scott's rule, as implemented in `scipy`. The resulting KDE is smooth in all three parameters when marginalizing over the range of the other parameters, suggesting it provides a fair representation of the prior information on the log(g) distribution. By combining the prior information on $T_{\rm eff}$ and [Fe/H] for each star (assuming Gaussian uncertainties) with this KDE, we construct the joint posterior probability for all three parameters:

$$\ln p(\log(g), T_{\rm eff}, [{\rm Fe/H}]) = \ln p({\rm KDE}(\log(g), T_{\rm eff}, [{\rm Fe/H}])) + \ln p(T_{\rm eff}) + \ln p([{\rm Fe/H}]), \quad ({\rm A1})$$

where KDE(log (g), $T_{\rm eff}$, [Fe/H]) is the density of the KDE at a given set of parameters, and $p(T_{\rm eff})$ and p([Fe/H]) are the prior information on $T_{\rm eff}$ and [Fe/H] from *SkyMapper*. For each star with missing log(g), we use rejection sampling to take samples of this posterior within the range of parameters represented in the full data set. We verify that this procedure gives a reliable constraint on log(g) by making an inference of the parameter for the set of stars with *TESS*-HERMES log(g) constraints, and find that the *SkyMapper* prior-based log(g) constraint is within 3σ of the *TESS*-HERMES measurement for all 1186 stars, and within 1σ for ~93 per cent of the sample. This suggests that this inference is reliable for the rest of the data set, and the resulting uncertainty on the log(g) constraint is realistic and will hence be propagated into our inference of luminosity, mass, age, and radii consistently. Fig. A1 shows the comparison between our inferred log(g) and that from *TESS*-HERMES. The median uncertainty on the inferred log(g) is 0.3, compared to 0.1 for the *TESS*-HERMES measurements.

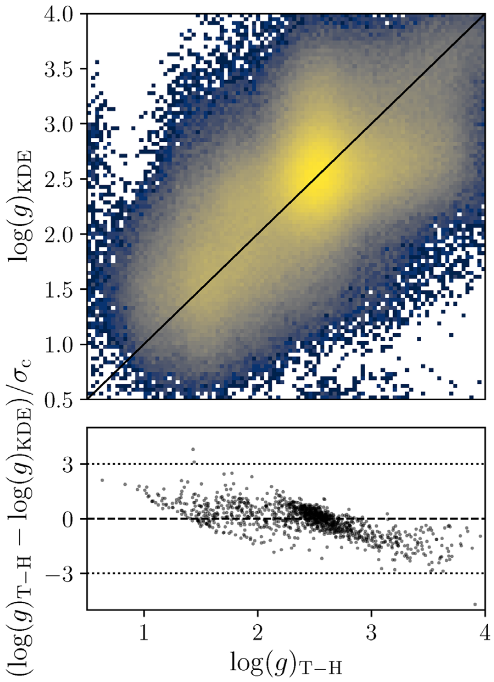

Figure A1. Comparison of log(g) from *TESS*-HERMES with that inferred using the *TESS*-HERMES and *SkyMapper* data as prior information. The top panel shows the density distribution of samples from the posterior, when the *TESS*-HERMES log g is used, and when the log(g) is inferred from the prior. The bottom panel compares the difference between the inferred and measured log(g), normalized by the combined uncertainty σ_c. ~93 per cent of the inferences of log(g) fall within 1σ of the measured values, although the uncertainty on the inferred log(g) is a factor of 3 greater than those measured by *TESS*-HERMES.

APPENDIX B: *GAIA* PARALLAX ZERO-POINT OFFSET

Since this sample represents an extension to brighter magnitudes of the set of stars with asteroseismic constraints, in a different region of the sky to previously available data (e.g. *Kepler*), it is appropriate to check if and how the derived parallax zero-point offset may change. While this is not the focus of this work and will likely form the basis of future, more detailed, studies based on *TESS* data, we make a simplified assessment of this offset here. Current assessments of the parallax zero-point offset in *Gaia* DR2 yield values of 30 µas $\lesssim \Delta\varpi \lesssim$ 60 µas (e.g. Lindegren et al. 2018; Hall et al. 2019; Khan et al. 2019; Leung & Bovy 2019; Schönrich et al. 2019; Zinn et al. 2019; Chan & Bovy 2020). Furthermore, it has been widely shown that the zero-point is multivariate as a function of position on the sky (e.g. Lindegren et al. 2018; Chan & Bovy 2020) and stellar parameters (e.g. Khan et al. 2019; Zinn et al. 2019).

Here, we make a simple assessment of the zero-point offset for the *TESS*-SCVZ sample only as a function of the apparent K_S-band magnitude. We take the raw *Gaia* DR2 parallax and its associated uncertainty, and derive a 'seismic' parallax by transforming the `PARAM` $M_{\rm bol}$ values, estimated using the BHM seismic parameters and the *SkyMapper* stellar parameters, using the bolometric corrections derived for the sample based also on these parameters. We use a separate run of `PARAM` that did not use the *Gaia* derived luminosity as a constraint such that the luminosity is directly predicted by the seismic and stellar parameters. We then sample the resultant posterior on $\Delta\varpi = \varpi_{\rm PARAM} - \varpi_{Gaia}$ and K_S for each star and use

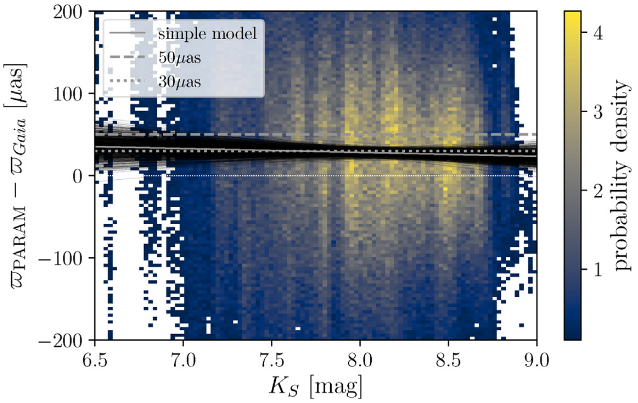

Figure B1. The *Gaia* DR2 parallax zero-point offset as a function of K_S magnitude, as measured by comparing the observed *Gaia* parallax values with those derived by measuring stellar luminosities using the BHM seismic results and PARAM (removing the constraint based on the *Gaia* luminosity). The 2D histogram shows the density of samples from the posteriors on magnitude and parallaxes, assuming Gaussian uncertainties. The dotted and dashed lines demonstrate the levels of common values for the zero-point offset measured using various techniques. Our best-fitting model is shown by the solid grey line, and MCMC samples of the posterior likelihood function of the parameters of the fit given the data are shown by the individual black lines. The best-fitting model gives a dependence of the offset on K_S of $\Delta\varpi = (-5 \pm 6)(K_S - 8) + (30 \pm 3)$ µas.

the 0.16, 0.5, and 0.84 quartiles as input to our fitting procedure. We use the likelihood function for a linear fit with two-dimensional uncertainties (assuming that the uncertainty on $\Delta\varpi$ and K_S are uncorrelated) given in equation 32 of Hogg, Bovy & Lang (2010), and sample the posterior distribution of the parameters describing a linear relationship between $\Delta\varpi$ and K_S using `emcee` (Foreman-Mackey et al. 2013).

The resulting fit and posterior samples compared to the data are shown in Fig. B1. The data are shown as a two-dimensional histogram of the samples from the posteriors on $\Delta\varpi$ and K_S, to give a sense of the large uncertainties on $\Delta\varpi$. Despite these large uncertainties, an offset of the mean $\Delta\varpi$ from 0 is clear. We show offsets of 30 and 50 µas as dotted and dashed lines, respectively, as a guide to how our derived offset compares with those from the literature. Our best-fitting model is consistent with being flat as a function of K_S, with a zero-point offset of ∼30 µas, such that $\Delta\varpi = (-5 \pm 6)(K_S - 8) + (30 \pm 3)$ µas. This offset is somewhat smaller than many derived using currently available asteroseismic samples (e.g. Hall et al. 2019; Khan et al. 2019; Zinn et al. 2019). This may be a genuine population effect, due to the fact that this sample is somewhat closer and thus brighter than the *Kepler* sample. This may also reflect noted variations as a function of position on the sky. Future studies of the *TESS* data will likely narrow down this estimation and trends with these parameters.

APPENDIX C: COMPARING PHOTOMETRIC AND ASTEROSEISMIC LUMINOSITIES

Fig. C1 shows the full comparison between $L_{\rm phot.}$ and $L_{\rm seis.}$ for each of the pipelines considered. We normalize the difference between $L_{\rm phot.}$ and $L_{\rm seis.}$ by the combined uncertainty on photometric and seismic luminosities σ_c. In this way, a difference of e.g. $3\sigma_c$ indicates the two measurements are consistent to 3σ. The uncertainty on $L_{\rm seis.}$ is considerably higher than that on $L_{\rm phot.}$ in many cases, which can lead to small values of this difference. However, since this indicates the uncertainties are well estimated, we allow these into our sample. The horizontal lines in each figure show the $\pm 3\sigma_c$ limit. For each pipeline, we colour the points by $\nu_{\rm max}$ and show (as larger points) the stars for which each pipeline returned a $\nu_{\rm max}$ close to the diurnal frequency ($\nu_{\rm max} = 11.57 \pm 0.1$). This will allow us to assess whether the appearance of these detections is real or due to some systematic in the *TESS* photometry.

Inspection of Fig. C1 reveals that there are a considerable number of targets across all three pipelines for which $L_{\rm seis.}$ is not consistent with $L_{\rm phot.}$ (within $3\sigma_c$). In each pipeline, a cloud of 'high' $\nu_{\rm max} \gtrsim 10^2$ detections is visible such that $L_{\rm seis.}$ underestimated by $\simeq 10\sigma_c$. This means that many intrinsically bright targets have been misidentified by the seismic analysis as high $\nu_{\rm max}$ and therefore low-luminosity stars. Visual inspection of the power spectra of a few of these targets shows that it appears that there is genuine power excess at low ν as expected from their luminosity. However, a number of features are apparent in the noisier, high ν part of the power spectrum. This likely indicates some fine-tuning of analysis methods may be necessary for *TESS* power spectra.

Furthermore, it appears that there are a number of genuine and photometrically consistent detections with $\nu_{\rm max} \simeq 11.57$ µ Hz, suggesting that systematics at this frequency are not as problematic as may be expected, given the scattered light present in many of the *TESS* observations. This also suggests that an apparent 'bump' in the $\nu_{\rm max}$ distribution at roughly this frequency may be a real feature.

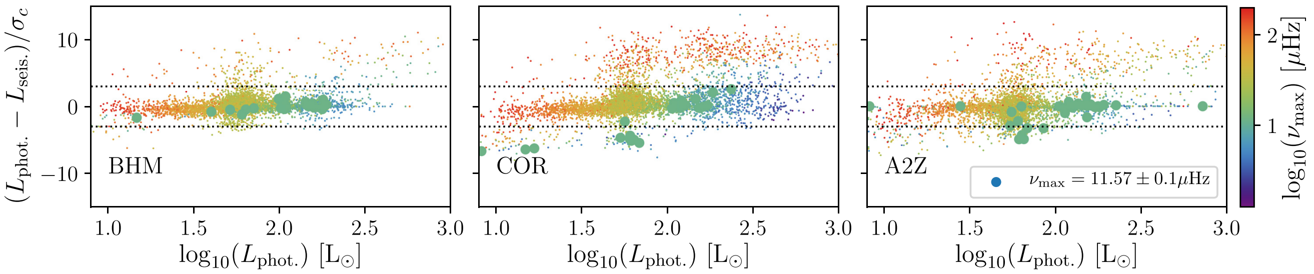

Figure C1. Comparison between photometrically and seismically derived luminosities. The seismic luminosities $L_{\rm seis.}$ are estimated using the scaling relations applied to the seismic parameters determined by the BHM, COR, and A2Z pipelines, from left to right. The vertical axes give the difference between photometric and seismic luminosity, normalized by the combined uncertainty σ_c. The dashed horizontal lines demonstrate the range at which results are consistent within $3\sigma_c$. The majority of stars have consistent luminosities in all three pipelines, but each have clear cases of false positive detections. We highlight stars with $\nu_{\rm max}$ near to the diurnal frequency (11.57 µHz) as larger points, demonstrating that most detections at this frequency appear to be true positives, and not due to systematic effects in our light curves.

APPENDIX D: CATALOGUE OF SEISMIC, PHOTOMETRIC, SPECTROSCOPIC, AND KINEMATIC PROPERTIES FOR *TESS*-SCVZ GIANTS

We provide all data necessary for the reproduction of the analyses presented here in a catalogue of the compiled seismic, photometric, spectroscopic, and kinematic properties for the 15 405 stars in the *TESS*-SCVZ bright red giant sample. The columns included in the data table are described in Table D1. All relevant columns described in Table D1 have associated uncertainties, which are adjacent to those columns in the table. The catalogue reproduces data produced by the *Gaia* (Gaia Collaboration 2018), 2MASS (Skrutskie et al. 2006), *TESS*-HERMES (Sharma et al. 2018), *SkyMapper* (Onken et al. 2019), and APOGEE (Majewski et al. 2017) surveys, and includes orbital parameters estimated as described in Section 2.

Since we include all the possible data in the catalogue (i.e. we do not remove stars that we flagged as bad in any way), we recommend that users take care to apply the appropriate selection to any data that is used. For example, we recommend that when using PARAM results, the sample is limited to only those stars with stellar radii measured to be less than $12R_{\odot}$ (as recommended by Miglio et al. 2021) and those with the appropriate luminosity flag indicating that the seismic parameters are robust relative to the *Gaia* luminosity. Furthermore, since the internal consistency is not optimal in this first set of data, we recommend that the mean $\nu_{\rm max}$ and $\Delta\nu$ values are avoided in most cases, as these can represent large deviations from the true values in some cases. Best practice might be to use a set of results from a single pipeline, restricting the sample to only those stars where consistent detections were made across all three pipelines (i.e. `numax_dnu_consistent` = 1), and where the relevant luminosity consistency flag is on (i.e. `lum_flag_XXX` = 1, where `XXX` is the relevant pipeline identifier). In the case of the BHM results, this provides a sample of 1749 stars that likely have the most robust data provided by that pipeline.

As an additional way to assess the data quality for individual targets, we include an estimate of the goodness of fit in `PARAM` through the χ^2 of the fit for those stars that returned parameter values. This value is computed by comparing the input constraints with those predicted by the best-fitting model. In this way, a star that is not well represented by the grid of stellar models employed by `PARAM` will have a high χ^2. We recommend that users check samples for high values of this parameter, especially when using small numbers of stars. Any χ^2 well above ∼4 (the number of degrees of freedom) can be considered to be a poor fit, and likely represent a star whose parameters are not reproduced by the models. Approximately 90 per cent of the targets with $\chi^2 > 4$ are removed by the flags outlined above. In the catalogue, these numbers are found under `CHI2_gof_PARAM_BHM` and `CHI2_gof_APO_PARAM_BHM` for the results using *SkyMapper* and APOGEE, respectively.

Table D1. The data model of the catalogue of *TESS*-SCVZ targets which we release in this work. We compile seismic, photometric, spectroscopic, and kinematic properties from *Gaia* (Gaia Collaboration 2018), 2MASS (Skrutskie et al. 2006), *TESS*-HERMES (Sharma et al. 2018), *SkyMapper* (Onken et al. 2019), and APOGEE (Majewski et al. 2017). Orbital parameters are computed using the method presented in Mackereth & Bovy (2018), implemented in `galpy` (Bovy 2015). All relevant columns are accompanied by an associated uncertainty, defined either as the standard deviation or the 0.16 and 0.84 quantiles. Uncertainties are found in accompanying columns labelled with the suffix '`err`'.

Column identifier	Description	Units
`source_id`	*Gaia* DR2 source ID	None
`N_sectors`	Number of sectors star was observed in	27 d
`ra`	Right ascension	deg
`dec`	Declination	deg
`l`	Galactic longitude	deg
`b`	Galactic latitude	deg
`ecl_lon`	Ecliptic longitude	deg
`ecl_lat`	Ecliptic latitude	deg
`parallax`	*Gaia* DR2 parallax	mas
`pmra`	*Gaia* DR2 proper motion in RA	mas yr^{-1}
`pmdec`	*Gaia* DR2 proper motion in Dec.	mas yr^{-1}
`radial_velocity`	*Gaia* DR2 heliocentric radial velocity	km s^{-1}
`hmag`	2MASS H-band magnitude	mag
`jmag`	2MASS J-band magnitude	mag
`kmag`	2MASS K_S-band magnitude	mag
`phot_g_mean_mag`	*Gaia* DR2 G-band magnitude	mag
`phot_bp_mean_mag`	*Gaia* DR2 G_{BP}-band magnitude	mag
`phot_rp_mean_mag`	*Gaia* DR2 G_{RP}-band magnitude	mag
`numax_COR`	$\nu_{\rm max}$ from COR pipeline	µHz
`dnu_COR`	$\Delta\nu$ from COR pipeline	µHz
`numax_BHM`	$\nu_{\rm max}$ from BHM pipeline	µHz
`dnu_BHM`	$\Delta\nu$ from BHM pipeline	µHz
`numax_A2Z`	$\nu_{\rm max}$ from A2Z pipeline	µHz
`dnu_A2Z`	$\Delta\nu$ from A2Z pipeline	µHz
`mean_numax`	Mean $\nu_{\rm max}$ between all pipelines returning results	µHz
`mean_dnu`	Mean $\Delta\nu$ between all pipelines returning results	µHz
`N_pipelines_mean`	Number of pipelines included in mean	None
`seismic_param_gold`	Flag indicating all pipeline results for $\nu_{\rm max}$ and $\Delta\nu$ within 1σ of global mean	Boolean
`logg_HERMES`	Surface gravity from *TESS*-HERMES	None
`Teff_SKYMAPPER`	$T_{\rm eff}$ from *SkyMapper*	K
`feh_SKYMAPPER`	[Fe/H] from *SkyMapper*	None
`ecc_MB2018`	Orbit eccentricity in `MWPotential2014`	None

Table D1 – *continued*

Column identifier	Description	Units
`rperi_MB2018`	Pericentre radius in `MWPotential2014`	kpc
`rap_MB2018`	Apocentre radius in `MWPotential2014`	kpc
`zmax_MB2018`	Maximum vertical excursion in `MWPotential2014`	kpc
`APOGEE_ID_APOGEE`	APOGEE ID in DR16	None
`FE_H_APOGEE`	APOGEE [Fe/H] (DR16)	None
`MG_FE_APOGEE`	APOGEE [Mg/Fe] (DR16)	None
`LOGG_APOGEE`	APOGEE $\log(g)$ (DR16)	None
`TEFF_APOGEE`	APOGEE $T_{\rm eff}$ (DR16)	K
`age_PARAM_BHM`	Age from PARAM, based on BHM and *SkyMapper*	Gyr
`mass_PARAM_BHM`	Mass from PARAM, based on BHM and *SkyMapper*	M$_\odot$
`rad_PARAM_BHM`	Radius from PARAM, based on BHM and *SkyMapper*	R$_\odot$
`CHI2_gof_PARAM_BHM`	χ^2 value from `PARAM` computed based on distance between input constraints and best-fitting model parameters	
`mbol_PARAM_BHM_NO_L`	Bolometric magnitude from PARAM, based on BHM and *SkyMapper* without using luminosity as a constraint	mag
`age_APO_PARAM_BHM`	Age from PARAM, based on BHM and APOGEE	Gyr
`mass_APO_PARAM_BHM`	Mass from PARAM, based on BHM and APOGEE	M$_\odot$
`rad_APO_PARAM_BHM`	Radius from PARAM, based on BHM and APOGEE	R$_\odot$
`CHI2_gof_APO_PARAM_BHM`	χ^2 value from `PARAM` computed based on distance between input constraints and best-fitting model parameters	
`luminosity_BHM`	Luminosity from seismic scaling relations applied to BHM	L$_\odot$
`luminosity_COR`	Luminosity from seismic scaling relations applied to COR	L$_\odot$
`luminosity_A2Z`	Luminosity from seismic scaling relations applied to A2Z	L$_\odot$
`luminosity_HERMES`	Luminosity based on 2MASS photometry and bolometric correction based on *TESS*-HERMES	L$_\odot$
`luminosity_GAIA`	Luminosity based on 2MASS photometry and bolometric correction based on *SkyMapper* and *Gaia* DR2 parallax	L$_\odot$
`luminosity_APO_GAIA`	Luminosity based on 2MASS photometry and bolometric correction based on APOGEE and *Gaia* DR2 parallax	L$_\odot$
`evstate_MV`	Evolutionary state using Vrard et al. (2016). RGB = 0, RC = 1, unclassified = −1	None
`lum_flag_BHM`	Luminosity flag for BHM – 1 if photometric and seismic luminosity agree within $3\sigma_c$	Boolean
`lum_flag_COR`	Luminosity flag for COR – 1 if photometric and seismic luminosity agree within $3\sigma_c$	Boolean
`lum_flag_A2Z`	Luminosity flag for A2Z- 1 if photometric and seismic luminosity agree within $3\sigma_c$	Boolean
`numax_dnu_consistent`	Quality flag, 1 if results on $\nu_{\rm max}$ and $\Delta\nu$ are consistent within 3σ across all pipelines	Boolean
`numax_predicted`	$\nu_{\rm max}$ predicted using 2MASS photometry and *Gaia* DR2 parallax	μHz

[1] *School of Astronomy and Astrophysics, University of Birmingham, Edgbaston, Birmingham B15 2TT, UK*
[2] *Canadian Institute for Theoretical Astrophysics, University of Toronto, 60 St. George Street, Toronto, ON M5S 3H8, Canada*
[3] *Dunlap Institute for Astronomy and Astrophysics, University of Toronto, 50 St. George Street, Toronto, ON M5S 3H4, Canada*
[4] *David A. Dunlap Department for Astronomy and Astrophysics, University of Toronto, 50 St. George Street, Toronto, ON M5S 3H4, Canada*
[5] *INAF – Astrophysics and Space Science Observatory Bologna, Via Gobetti 93/3, I-40129 Bologna, Italy*
[6] *LESIA, Observatoire de Paris, Université PSL, CNRS, Sorbonne Université, Université de Paris, 5 place Jules Janssen, F-92195 Meudon, France*
[7] *Instituto de Astrofísica de Canarias, E-38205, La Laguna, Tenerife, Spain*
[8] *Dpto. de Astrofísica, Universidad de La Laguna, Avda. Astrofísico Francisco Sánchez, E-38206 La Laguna, Tenerife, Spain*
[9] *IRFU, CEA, Université Paris-Saclay, F-91191 Gif-sur-Yvette, France*
[10] *AIM, CEA, CNRS, Université Paris-Saclay, Université Paris Diderot, Sorbonne Paris Cité, F-91191 Gif-sur-Yvette, France*
[11] *Aix Marseille Univ, CNRS, CNES, LAM, 13388 Marseille Cedex 13, France*
[12] *Istituto Nazionale Astrofisica di Padova – Osservatorio Astronomico di Padova, Vicolo dell'Osservatorio 5, I-35122 Padova, Italy*
[13] *Department of Astronomy, The Ohio State University, 140 W. 18th Ave., Columbus, OH 43210, USA*
[14] *Department of Astronomy, Yale University, New Haven, CT 06520, USA*
[15] *Department of Astrophysical Sciences, Princeton University, 4 Ivy Lane, Princeton, NJ 08544, USA*
[16] *The Observatories of the Carnegie Institution for Science, 813 Santa Barbara St., Pasadena, CA 91101, USA*
[17] *Institut für Physik, Universität Graz, Universitätsplatz 5/II, A-8020 Graz Austria*
[18] *Max-Planck Institut für Astronomie, Königstuhl 17, D-69117 Heidelberg, Germany*
[19] *Instituto de Astrofísica e Ciências do Espaço, Universidade do Porto, Rua das Estrelas, P-4150-762 Porto, Portugal*
[20] *Research School of Astronomy and Astrophysics, Mount Stromlo Observatory, The Australian National University, Cotter Road, Weston Creek, ACT 2611, Australia*
[21] *Departamento de Física e Astronomia, Faculdade de Ciências da Universidade do Porto, Rua do Campo Alegre, s/n, P-4169-007 Porto, Portugal*
[22] *Leibniz-Institut für Astrophysik Potsdam (AIP), An der Sternwarte 16, D-14482 Potsdam, Germany*
[23] *Department of Astronomy, The Ohio State University, Columbus, OH 43210, USA*
[24] *Institute of Space Sciences (ICE, CSIC), Carrer de Can Magrans S/N, E-08193 Bellaterra, Spain*
[25] *Institut d'Estudis Espacials de Cataluna (IEEC), Carrer Gran Capita 2, E-08034 Barcelona, Spain*
[26] *Stellar Astrophysics Centre, Department of Physics and Astronomy, Aarhus University, Ny Munkegade 120, DK-8000 Aarhus C, Denmark*
[27] *School of Physics, University of New South Wales, Kensington, NSW 2052, Australia*
[28] *Institute for Astronomy, University of Hawai'i, 2680 Woodlawn Drive, Honolulu, HI 96822, USA*
[29] *Carnegie Earth and Planet Laboratory, 5241 Broad Branch Road, N.W., Washington, DC 20015, USA*
[30] *The Observatories of the Carnegie Institution for Science, 813 Santa Barbara St., Pasadena, CA 91101, USA*